NAVAL POSTGRADUATE SCHOOL

MONTEREY, CALIFORNIA

THESIS

REMOVAL OF DIRECT CURRENT LINK HARMONIC RIPPLE IN SINGLE-PHASE VOLTAGE SOURCE INVERTER SYSTEMS USING SUPERCAPACITORS

by

Gabriel D. Hernandez

September 2016

Thesis Advisor:	Giovanna Oriti
Co-Advisor:	Alexander L. Julian
Second Reader:	Roberto Cristi

THIS PAGE INTENTIONALLY LEFT BLANK

REPORT DOCUMENTATION PAGE			*Form Approved OMB No. 0704-0188*
Public reporting burden for this collection of information is estimated to average 1 hour per response, including the time for reviewing instruction, searching existing data sources, gathering and maintaining the data needed, and completing and reviewing the collection of information. Send comments regarding this burden estimate or any other aspect of this collection of information, including suggestions for reducing this burden, to Washington headquarters Services, Directorate for Information Operations and Reports, 1215 Jefferson Davis Highway, Suite 1204, Arlington, VA 22202-4302, and to the Office of Management and Budget, Paperwork Reduction Project (0704-0188) Washington DC 20503.			
1. AGENCY USE ONLY ***(Leave blank)***	**2. REPORT DATE** September 2016	**3. REPORT TYPE AND DATES COVERED** Master's thesis	
4. TITLE AND SUBTITLE REMOVAL OF DIRECT CURRENT LINK HARMONIC RIPPLE IN SINGLE-PHASE VOLTAGE SOURCE INVERTER SYSTEMS USING SUPERCAPACITORS			**5. FUNDING NUMBERS**
6. AUTHOR(S) Gabriel D. Hernandez			
7. PERFORMING ORGANIZATION NAME(S) AND ADDRESS(ES) Naval Postgraduate School Monterey, CA 93943-5000			**8. PERFORMING ORGANIZATION REPORT NUMBER**
9. SPONSORING /MONITORING AGENCY NAME(S) AND ADDRESS(ES) N/A			**10. SPONSORING / MONITORING AGENCY REPORT NUMBER**
11. SUPPLEMENTARY NOTES The views expressed in this thesis are those of the author and do not reflect the official policy or position of the Department of Defense or the U.S. Government. IRB Protocol number ____N/A____.			
12a. DISTRIBUTION / AVAILABILITY STATEMENT Approved for public release; distribution is unlimited			**12b. DISTRIBUTION CODE**

13. ABSTRACT (maximum 200 words)

For an Energy Management System (EMS)-controlled microgrid that uses a single-phase voltage source inverter (VSI) configuration to supply power for AC loads from DC energy storage devices, the DC link connecting the VSI to the DC energy storage devices experiences a voltage ripple that is a second-order harmonic of the AC frequency. When the EMS has a battery bank as the only DC energy storage device, the DC link voltage ripple causes a second-order harmonic ripple in battery current that leads to a reduction in battery life. Supercapacitors (SCs), which are capable of operating through many more cycles than batteries, can be added to the EMS to form a battery and SC Hybrid Energy Storage System (HESS). The EMS can then be used to filter out the second-order harmonic ripple in battery bank current and provide this current solely from the SC bank, extending battery life and reducing system operating costs.

The design of a computer simulation of an EMS providing power to a microgrid is discussed in this thesis. Simulations provide theoretical results and laboratory results compare well with the theoretical results, showing that SCs can be used to remove the second-order harmonic current ripple from the battery bank.

14. SUBJECT TERMS Energy Management System (EMS), peak shaving, Voltage Source Inverters (VSI), Hybrid Energy Storage System (HESS), supercapacitor (SC), ultracapacitor (UC), power electronics, microgrid (MG), bidirectional dc/dc converters, battery life extension			**15. NUMBER OF PAGES** 89 / **16. PRICE CODE**
17. SECURITY CLASSIFICATION OF REPORT Unclassified	**18. SECURITY CLASSIFICATION OF THIS PAGE** Unclassified	**19. SECURITY CLASSIFICATION OF ABSTRACT** Unclassified	**20. LIMITATION OF ABSTRACT** UU

NSN 7540-01-280-5500

Standard Form 298 (Rev. 2-89)
Prescribed by ANSI Std. 239-18

THIS PAGE INTENTIONALLY LEFT BLANK

Approved for public release; distribution is unlimited

REMOVAL OF DIRECT CURRENT LINK HARMONIC RIPPLE IN SINGLE-PHASE VOLTAGE SOURCE INVERTER SYSTEMS USING SUPERCAPACITORS

Gabriel D. Hernandez
Lieutenant Commander, United States Navy
B.S., University of California at Davis, 2004

Submitted in partial fulfillment of the
requirements for the degree of

ELECTRICAL ENGINEER
AND
MASTER OF SCIENCE IN ELECTRICAL ENGINEERING

from the

NAVAL POSTGRADUATE SCHOOL
September 2016

Approved by: Giovanna Oriti
Thesis Advisor

Alexander L. Julian
Co-Advisor

Roberto Cristi
Second Reader

R. Clark Robertson
Chair, Department of Electrical and Computer Engineering

THIS PAGE INTENTIONALLY LEFT BLANK

ABSTRACT

For an Energy Management System (EMS)-controlled microgrid that uses a single-phase voltage source inverter (VSI) configuration to supply power for AC loads from DC energy storage devices, the DC link connecting the VSI to the DC energy storage devices experiences a voltage ripple that is a second-order harmonic of the AC frequency. When the EMS has a battery bank as the only DC energy storage device, the DC link voltage ripple causes a second-order harmonic ripple in battery current that leads to a reduction in battery life. Supercapacitors (SCs), which are capable of operating through many more cycles than batteries, can be added to the EMS to form a battery and SC Hybrid Energy Storage System (HESS). The EMS can then be used to filter out the second-order harmonic ripple in battery bank current and provide this current solely from the SC bank, extending battery life and reducing system operating costs.

The design of a computer simulation of an EMS providing power to a microgrid is discussed in this thesis. Simulations provide theoretical results and laboratory results compare well with the theoretical results, showing that SCs can be used to remove the second-order harmonic current ripple from the battery bank.

THIS PAGE INTENTIONALLY LEFT BLANK

TABLE OF CONTENTS

LIST OF FIGURES

THIS PAGE INTENTIONALLY LEFT BLANK

LIST OF ACRONYMS AND ABBREVIATIONS

AC	alternating current
BBC	buck-boost converter
BPF	band-pass filter
CCM	continuous conduction mode
CNO	Chief of Naval Operations
CT	current threshold
DC	direct current
DCM	discontinuous conduction mode
DOD	Department of Defense
DON	Department of the Navy
DR	distributed resources
EMS	energy management system
FPGA	field-programmable gate array
HESS	hybrid energy storage system
IGBT	insulated gate bipolar transistor
KCL	Kirchhoff's Current Law
KVL	Kirchhoff's Voltage Law
LPF	low-pass filter
OPNAV	Office of the Chief of Naval Operations
PHD	doctor of philosophy
PI	proportional integral
PV	photovoltaic
PWM	pulse-width modulation
SC	supercapacitor
SECNAV	Secretary of the Navy
USMC	United States Marine Corps
VRLA	valve-regulated lead acid
VSI	voltage source inverter

THIS PAGE INTENTIONALLY LEFT BLANK

ACKNOWLEDGMENTS

To Professors Giovanna Oriti, Alexander Julian, and Roberto Cristi, I extend my sincere appreciation for all of the time that you have spent in helping me to develop this thesis. Throughout this process, I was well aware of the fact that I was constantly standing on the shoulders of giants.

To my beautiful wife, Zuleika, I am forever indebted to you for your constant support and love throughout all of our experiences together. If I am ever considered to have had success in any aspect of my naval career, it is because you have always been by my side.

To my son, Julian, you are a joy to be around every day, and I look forward to helping you continue to learn and grow for the rest of my life. You and your mother are truly the loves of my life.

THIS PAGE INTENTIONALLY LEFT BLANK

I. INTRODUCTION

The Navy Shore Energy Program lists energy bills as "the single largest cost for Navy installations, reflecting about 28% of Navy's shore budget" [1]. The importance of efficient production and use of energy throughout the Department of Defense (DOD), exacerbated by the increasingly tight fiscal constraints felt throughout all elements of the president's Budget in recent years, has led the DOD to focus heavily on energy management. As a direct result of these increased concerns, the office of the Deputy Assistant Secretary of the Navy (Energy) was established along with several energy organizations such as the Department of the Navy's (DON) "Task Force Energy" and the United States Marine Corps (USMC) "Expeditionary Energy" program. Together, these groups strive to achieve the energy goals set forth by the Secretary of the Navy (SECNAV) and laid out in the Office of the Chief of Naval Operations (OPNAV) instruction 4100.5E, "Shore Energy Management," including the plan to provide 50% of all shore-based energy requirements from alternative sources by the year 2020 [2]. Adding alternative energy sources and multiple energy storage methods to local grids on installations will increase our energy efficiency and power reliability, but this will require more advanced energy management techniques to handle the distributed resources (DR) providing power to a grid.

A. PURPOSE

Energy Management System (EMS) technology has gained much popularity in recent years [3], [4], [5], [6], particularly in allowing the control of DR that are part of a microgrid. A microgrid is "a cluster of micro-sources, storage systems and loads which presents itself to the grid as a single entity that can respond to central control signals" [7], where the micro-sources can include sources such as micro-turbines and battery banks. Among the many benefits provided by an EMS is the ability to allow efficient and reliable sharing of grid loads by several disparate power sources, which allows alternative energy sources such as solar and wind energy to provide power to installation loads alongside more traditional power sources such as diesel generators. The EMS also allows

for the concurrent use of several different energy storage methods, maximizing an installation's energy efficiency and cost effectiveness.

The use of traditional batteries as the sole energy storage method in a microgrid is plagued by cost and reliability issues. Batteries are often quite expensive to purchase and replace, and there are many factors such as temperature, number of discharge cycles, and depth of discharge that can negatively affect battery service life. For an Energy Management System (EMS)-controlled microgrid that uses a single-phase voltage source inverter (VSI) configuration and a battery bank for energy storage, the DC link connecting the VSI to the battery bank experiences a voltage ripple that causes a corresponding ripple in battery bank current, leading to a reduction in battery life and increased system operating costs. This DC link voltage ripple, which is a second-order harmonic of the AC load frequency, is caused by the use of the VSI to convert DC to AC and will result in a second-order harmonic ripple in battery current unless the EMS is configured to filter out this ripple current from the battery bank and provide it from another source. Supercapacitors (SCs) can be added to the EMS to form a battery and SC Hybrid Energy Storage System (HESS). The EMS can then be used to filter out the second-order harmonic ripple in battery bank current and provide this current solely from the SC bank, extending battery life and reducing system operating costs. As stated in [8], electric double-layer capacitors known as SCs have desirable short-term energy storage and power properties when compared with batteries, making them an attractive option for hybrid energy storage systems (HESSs). While SCs have a lower energy density than batteries, they have a higher power density than batteries and can provide very high output power (on the order of hundreds of kW) for seconds at a time [8]. In addition to their high power density, SCs have an increased life cycle and can operate through many more charge and discharge cycles than traditional batteries (more than 100,000 [8]) before requiring replacement.

In this thesis, one method of employing an EMS to provide and control installation power using a battery and SC HESS is covered, where the system is configured as a parallel power source with the main grid. The focus is on showing how the use of a battery and SC HESS reduces battery ripple current, which can maximize

battery lifetime and ultimately reduce the amount of money that the DOD spends on energy for its installations each year. A computer simulation of the grid providing power to a microgrid via an EMS and employing a battery and SC HESS clearly shows the functionality of the system. The theoretical results of these simulations are confirmed by laboratory experimentation.

B. RESEARCH OBJECTIVES

The primary research objective of this thesis is to show, using both simulation and experiment, that, when using an EMS on a microgrid with a single-phase Voltage Source Inverter (VSI), the battery bank ripple current caused by the second-order harmonic DC link voltage ripple can be filtered out by adding an SC bank with a band pass filter (BPF) and associated control circuitry to the system. In exploring the primary objective, a secondary objective is to determine if the battery ripple current can be further minimized by adding an additional low pass filter (LPF), leaving essentially only DC current on the battery bus in steady state.

C. RELATED WORK

There are several examples in the literature, such as [9], [10], [11], and [12], of a battery and SC HESS used in grid-connected applications and controlled by an inverter-based EMS. While the benefits achievable by using this energy storage scheme are well understood, there are many different opinions on how to best design the power control system to achieve maximum efficiency and battery life extension. Various methods, including the use of fuzzy logic control [13], inner-loop current and outer-loop voltage control [12], and model-predictive-based control [14] have been covered in great detail. The approach chosen in this thesis differs from those found in literature in the way that the system model is built and analyzed and in the way that battery and SC current and power are controlled. Another focus found in much of the related literature is to find a way to quantify the amount of battery life extension achieved via the use of an EMS and HESS. In [15], Shen et al. use a battery life degradation model to optimize battery cycles in an electric vehicle with a battery and SC HESS. In [16], models are analyzed by calculating the parameters that affect battery performance and comparing the differences

in these values between different models and configurations. The specific estimates of battery life extension afforded by using the system that is described are not covered in detail, but the observations in the aforementioned literature and the general notion that reducing battery ripple current (cycles) leads to an extension in battery life are relied upon.

II. ENERGY MANAGEMENT SYSTEM WITH HYBRID ENERGY STORAGE

In order to understand the operation of the EMS as employed in this thesis, it is necessary to learn about its architecture, including power converters and control systems. The requisite background information is provided in this section.

A. SYSTEM OVERVIEW AND DESCRIPTION

In this section, an in-depth overview is provided of the EMS that is used in both simulations and laboratory experimentation. The circuit diagram of a microgrid with a HESS and EMS is provided, and the simulation circuitry is derived directly from this diagram.

1. Physical System Overview

The EMS used for this thesis is a power electronics-based system designed to control and manage energy sources and storage on a microgrid. A microgrid is a "local energy grid with control capability that can disconnect from a main grid (where it is connected at the point of common coupling) for autonomous operation" [17]. The main components of the EMS, shown in Figure 1, are the EMS logic circuitry, the primary controller, and the Insulated Gate Bipolar Transistor (IGBT) power module.

a. EMS Logic Circuitry

An external secondary controller, which provides an interface for the operator to control various system parameters based on chosen settings, provides input signals to the EMS logic circuitry. The logic circuitry performs computations on these signals, producing control signals that are used to direct EMS operations. The logic circuitry can set the load current peak-shaving limit, connect or disconnect the EMS output to and from the grid, perform reactive power compensation, shed non-critical loads and determine the direction of power flow to manage the HESS. A complete description of the operation of this logic circuitry is given in [18].

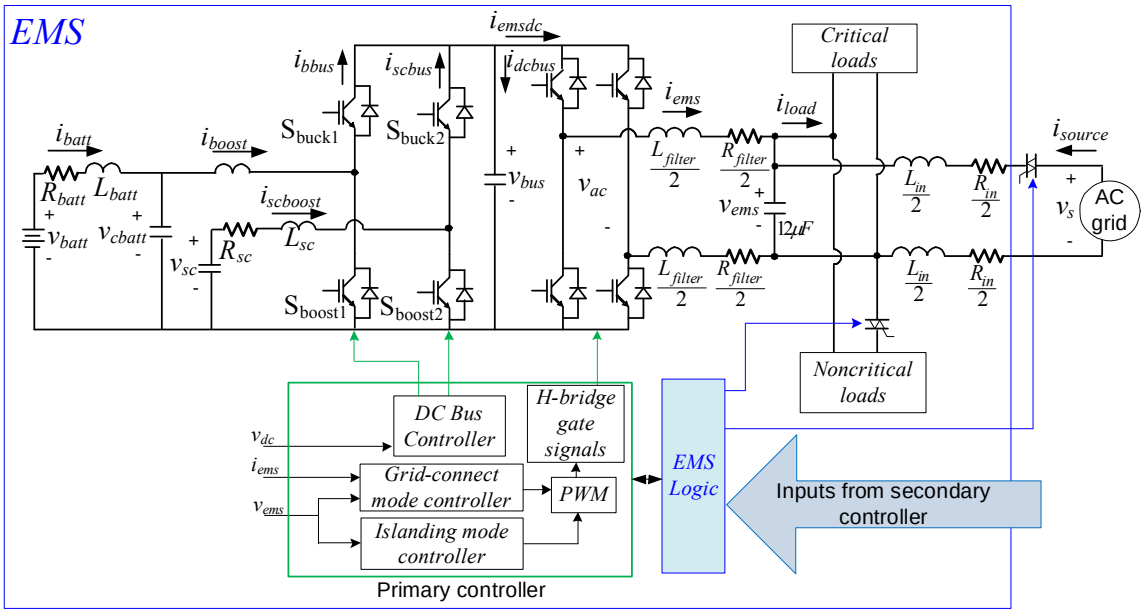

Figure 1. EMS Schematic. Adapted from [18].

b. Primary Controller

The primary controller module consists of current and voltage controllers for the different operating modes of the EMS. The output of these controllers is used to produce a signal that acts as a reference value for the pulse-width modulation (PWM) circuitry, which gates the inverter H-bridge IGBTs so that the DC bus can provide the required AC voltage and current to the loads. A DC bus controller is used to control the IGBTs in two bi-directional buck/boost converters (BBCs) and control the power drawn from the battery and SC modules as well as to allow for battery and SC charging when desired. By employing BBCs between the battery and SC banks, we see that the system is arranged as an actively controlled HESS. Another possible configuration is to directly connect the SC bank in parallel with the battery bank in what is known as a passive HESS. In this configuration, battery and SC bank power sharing is controlled by the battery bank terminal voltage, along with battery and SC internal resistance. Active and passive HESS configurations are shown in Figure 2 and Figure 3, respectively. As shown in [19], the actively controlled configuration has several benefits, such as a much higher power

capability, a larger output voltage range, better voltage regulation, and smaller system weight and volume (among other benefits), and it is the configuration chosen for this thesis.

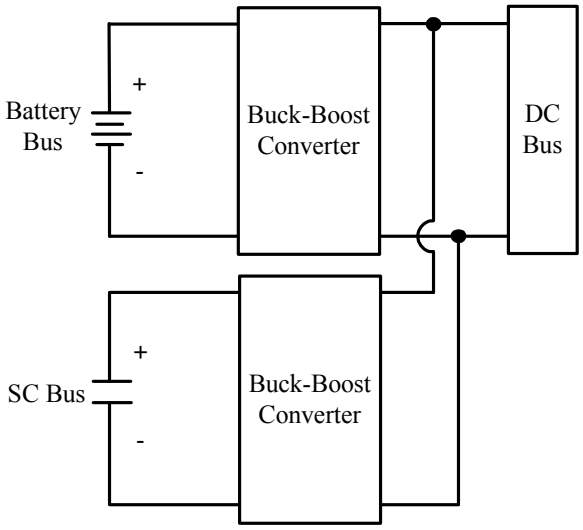

Figure 2. Active HESS Configuration

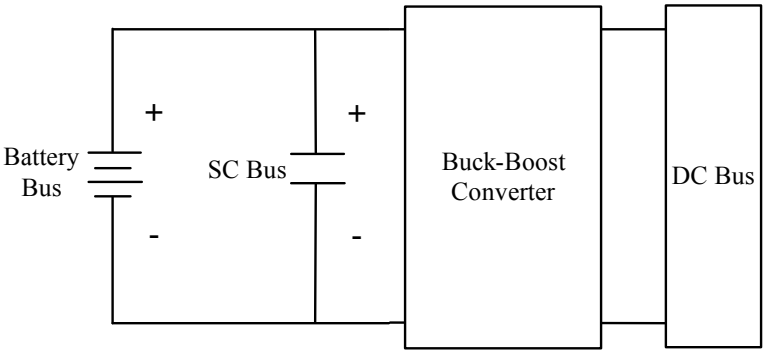

Figure 3. Passive HESS Configuration

c. IGBT Power Module

The IGBT power module consists of four IGBTs for the H-bridge inverter and two IGBTs for each of the two BBCs between the DC bus (labeled v_{bus} in Figure 1) and the battery and SC banks, for a total of eight IGBTs. The BBC IGBTs receive their gate signals from the primary controller, which modulates them to control v_{bus} and the charge

signal from the secondary controller (when battery charging is desired). The H-bridge IGBTs receive their gate signals from either the grid-connected or islanding mode controller (depending on mode of EMS operation), which modulates them to provide AC current to the loads.

d. Modes of Operation

The EMS can operate in either the grid-connected or islanding mode, based on an input from the secondary controller. As described in [18], the secondary controller provides four logical commands to the EMS:

- Run–This command is, in effect, an "On-off" switch for the EMS. When Run is low, the EMS is not operational. Once Run is shifted to high, the EMS operates to provide power to system loads.
- Source Connect–When Run is high, the value of Source Connect determines whether or not the AC grid is connected to v_{ac}, the AC output voltage of the EMS. If Source Connect is low, the source is not connected. If Source Connect is high and the source RMS voltage is sufficiently high (100 v_{rms}), a thyristor is gated shut to connected the source to v_{ac}.
- Current Threshold (CT)–This signal sets the load current at which the EMS uses the HESS to conduct peak shaving, reducing the power peaks supplied by the source.
- Charge–This signal, when set to high, causes the BBC between the DC bus and the battery bank to operate in buck mode, charging the battery bank from the source. In order for charging to occur, the load current must be less than the CT (indicating that peak shaving is not desired).

Each of the four logical commands described above can be manually entered by an operator or automatically generated based on system conditions. Together, they define the operating mode of the EMS.

(1) Grid-Connected Mode

In grid-connected mode, Run is set to high on the secondary controller, Source Connect is set to high, and AC grid voltage is at least 100 V_{rms}. This allows the HESS to share system loads with the AC grid, providing power as necessary during load increases.

(2) Islanding Mode

In islanding mode, Run is set to high on the secondary controller but either Source Connect is low or the AC grid voltage is not at least 100 V_{rms}, making it insufficient to provide reliable power to critical loads. This operating mode is in effect when the AC grid is lost and the EMS provides power from the HESS to system loads.

2. Components

The bi-directional BBC, as depicted in Figure 4, operates as a boost converter when the buck switch is open and the boost switch is modulated or as a buck converter when the boost switch is open and the buck switch is modulated. This method of connecting the battery and SC banks to the DC bus allows power flow in either direction while the DC bus and HESS are operating at different voltages. The amount by which the DC bus and the HESS voltages differ determines the desired switch modulation duty cycle.

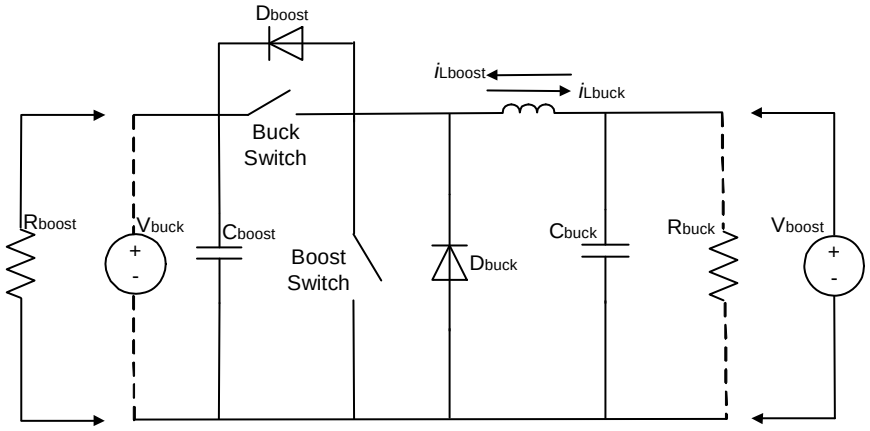

Figure 4. Bi-directional BBC

The operation of the BBC connecting the battery bank to the DC bus is shown in Figure 5. When operating as a boost converter, the buck switch (labeled S_{buck1}) is open while the boost switch (labeled S_{boost1}) is modulated. Shutting S_{boost1} causes the source to store energy in the inductor by increasing the inductor current. Once S_{boost1} is opened, the inductor voltage instantly switches polarity and increases as necessary in an attempt to

maintain the inductor current constant, which "boosts" the converter output voltage to the desired value and power is provided to the DC bus at v_{bus}.

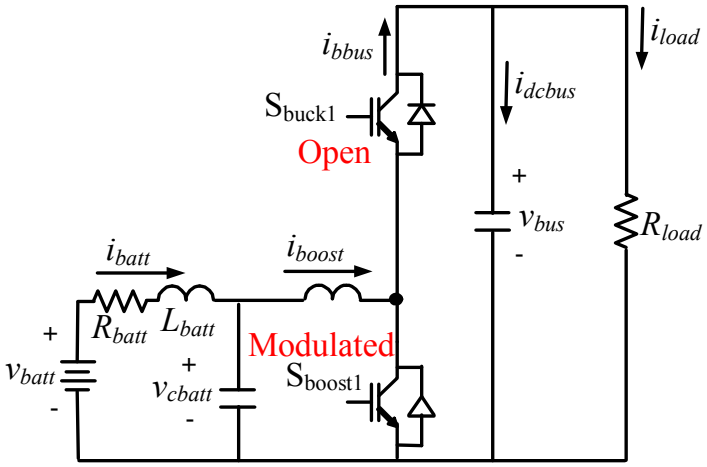

Figure 5. Battery Bank Boost Schematic

When operating as a buck converter, the BBC allows for the battery or SC bank to be charged by the DC bus, despite the fact that the DC bus is operating at a higher voltage (200 V) than either bank. In this configuration, S_{buck1} is modulated and S_{boost1} is kept open, as shown in Figure 6.

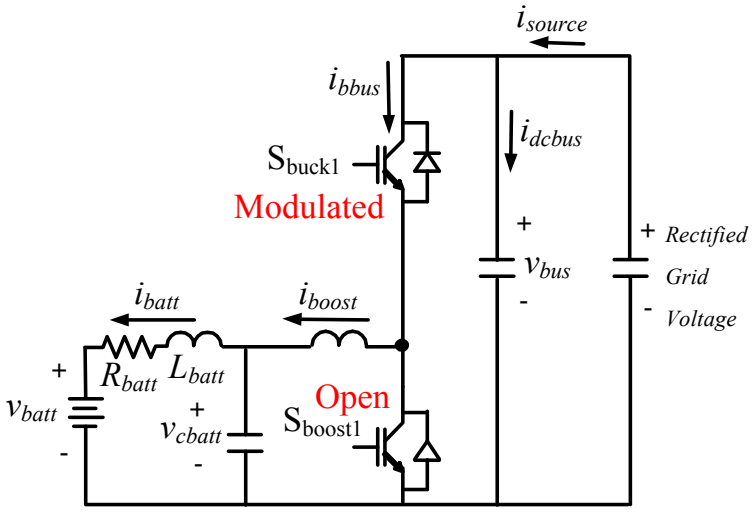

Figure 6. Battery Bank Buck Schematic

Shutting S_{buck1} causes the DC bus (source) to store energy in the inductor by increasing inductor current and providing current to the batteries and SCs to charge the desired bank. Opening S_{buck1} allows current flowing to the selected bank to dissipate, reducing charging power flow. By controlling the duty cycle of S_{buck1}, we maintain the desired charge rate at the desired voltage.

a. Supercapacitors

Electric double-layer capacitors, also called supercapacitors (SCs), have become very popular in recent years. To understand the benefits of employing SCs in an EMS HESS instead of conventional capacitors, it is important to understand the differences between these two devices.

(1) Traditional (Electrolytic) Capacitor Theory

An electrolytic capacitor is a device constructed of a dielectric material (which does not conduct electricity but can store energy by becoming polarized) sandwiched between two electrodes. As a voltage is applied across the capacitor, the charge Q stored in the electrostatic field between the positive and negative electrodes is

$$Q = CV\,, \tag{1}$$

where C is the capacitance and V is the voltage across the SC. The capacitance is measured in farads and given by

$$C = \varepsilon_o \frac{A}{d}\,, \tag{2}$$

where ε_o is the permittivity of free space, A is the area of the electrode in m^2, and d is the distance between the two electrodes in m. It can be seen that the amount of charge a traditional electrostatic capacitor can store is dictated by the area of the electrodes and the distance between them. The energy E that is stored in a capacitor, directly related to the amount of charge that the device can store and the type of dielectric material chosen, is

$$E = \frac{1}{2} CV^2\,. \tag{3}$$

(2) Supercapacitor Theory

While SCs, also known as ultracapacitors, are electrochemical capacitors that store charge using a different method than that used by conventional capacitors, they are governed by the same basic charge, capacitance, and energy equations. As described in [8] and shown in Figure 7, supercapacitors are constructed of two porous electrodes, separated by an ion-conductive membrane, in electrolyte solution.

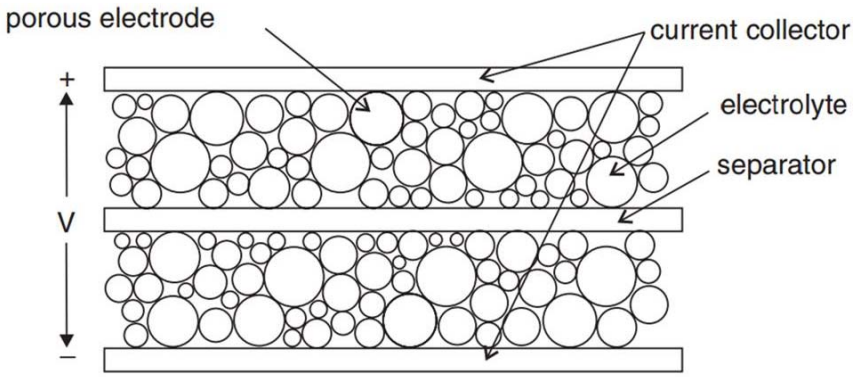

Figure 7. Supercapacitor Construction. Source: [8].

A complex electrochemical reaction occurs at the boundary between the pores in the electrodes and the electrolyte (where energy is stored), which displaces ions that diffuse through the electrolyte and the separating membrane between the electrodes. Due to the large surface area of the electrodes, SCs can store much more charge and attain much higher capacitance than traditional capacitors.

There are many possible mathematical models used for an SC, ranging from very complex models, such as the one described in [20], to simpler models, such as the dynamic model described and used in [21]. The dynamic model of a supercapacitor used for simulations in this thesis, which includes an ideal capacitor and an equivalent series resistance (R_{sc}), is shown in Figure 8. This model ignores the effect of temperature, frequency, and voltage changes on R_{sc} over time, but since the SC equivalent series resistance is unaffected by the discharge depth, as described in [22], this model is sufficiently accurate for the descriptions in this thesis.

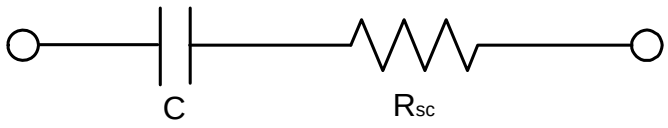

Figure 8. SC Dynamic Model

b. Single-Phase Voltage Source Inverter (H-Bridge)

The single-phase, H-bridge VSI has properties that are unique to single-phase systems that are directly responsible for the generation of battery ripple current. A description of this system is necessary to understand the cause and solution of this problem.

(1) General Description

Figure 9 is a depiction of the H-bridge inverter used in the EMS. The four IGBTs of the circuit are gated by the pulse-width modulated output from the grid-connected or islanding mode controller (depending on EMS operating mode) to control the direction of power flow between the AC grid and the HESS.

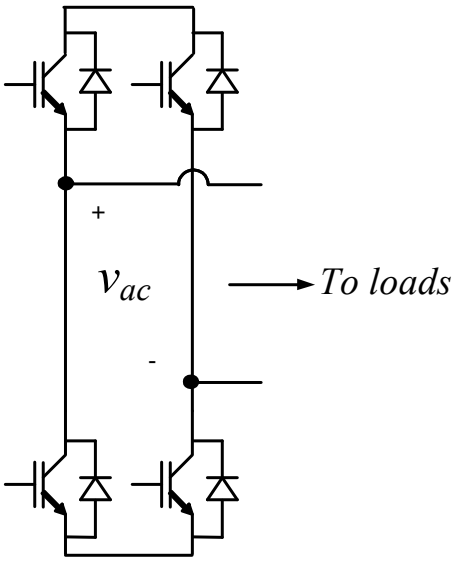

Figure 9. H-Bridge Inverter Schematic

(2) Second-Order Harmonic DC Link Voltage Ripple

A common problem associated with the use of single-phase systems employing PWM H-bridge inverters is the introduction of a second-order harmonic voltage ripple (at twice the AC load frequency) on the DC link (v_{bus}). In the case of an EMS employing a battery-only energy storage system, this ripple is passed directly to the battery bank current, which leads to rapid battery cycling and shortened battery life. The source of this harmonic ripple is found by examining the EMS power output

$$p_{out} = v_{ac} i_{ems} \ , \tag{4}$$

where both v_{ac} and i_{ems} are 60 Hz AC sine waves (voltage and current) for the 60 Hz loads. Multiplying these two 60 Hz sine waves produces a 120-Hz sine wave component of output power, as we can see from the well-known trigonometric identity

$$sin^2\theta = \frac{1 - cos(2\theta)}{2} \ . \tag{5}$$

The $cos(2\theta)$ second-order harmonic power term is reflected across the H-bridge inverter and causes a 120-Hz ripple in v_{bus}. The power provided by the battery bank is

$$P_{batt} = v_{batt} i_{batt} \ , \tag{6}$$

where v_{batt} and i_{batt} are battery voltage and battery current, respectively. The battery bank maintains essentially a constant voltage in the short-term and is assumed to be constant for the purpose of simulations in this thesis. As such, the 120-Hz second-order harmonic ripple is translated directly to the battery bus current. This harmonic increases the current seen by energy storage devices, which leads to heating of components and a reduction in battery life. Often, as described in [23] and [24], complex and expensive ripple reduction circuitry or parallel capacitances are added to the DC link to remove this ripple. Another method for removing this second-order (120-Hz) harmonic, which takes advantage of the SCs in the HESS and the ability of the EMS to schedule individual source currents, is presented in this thesis.

B. HYBRID ENERGY STORAGE SYSTEM

In this thesis, we focus on a HESS that makes use of lead-acid batteries and SCs.

1. General Description

The application of an EMS provides the ability to use multiple energy storage methods on a microgrid by allowing control of when and how power is provided from each storage device. Devices are selected based on their characteristics, providing an overall system that best suits the expected load profile. Two of the primary factors to consider when selecting an energy storage scheme are the power density and energy density of the chosen devices.

2. Benefits of Using Supercapacitors

As shown in Figure 10, SCs are capable of offering a higher power density than batteries, allowing them to provide power for large or fast load changes. This, in combination with the ability to operate with high efficiency through a large number of operating cycles (on the order of 100,000 [8]), makes SCs ideal for use in a HESS with peak shaving and high pulse-power applications.

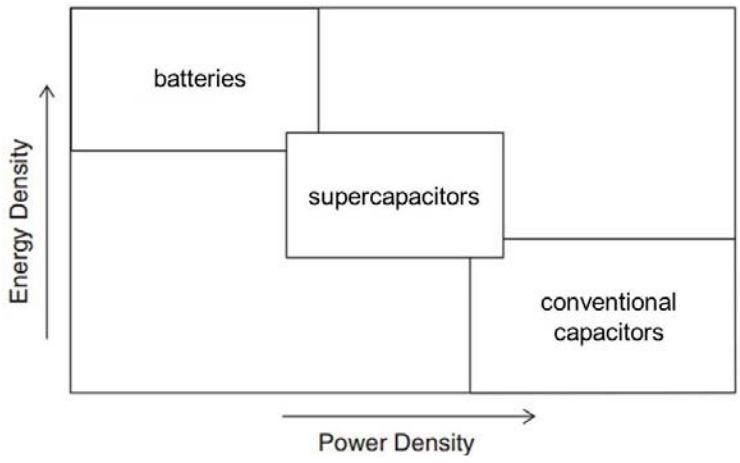

Figure 10. Simplified Ragone Chart Comparing Batteries, SCs and Capacitors. Adapted from [8].

SCs have a higher energy density than traditional capacitors, so they are able to provide power for a longer period of time before requiring a recharge. This allows the SCs to shave longer power peaks than traditional capacitors, again reducing the cycles seen by the HESS batteries. Overall, the combination of batteries and SCs results in a

HESS that has a higher overall power density than a battery-only energy storage system and a higher overall energy density than a battery and capacitor HESS.

a. Peak Shaving

With an EMS and a battery-only energy storage scheme, the power distribution system can be configured to allow the batteries to supply power during large load changes that result in power peaks [18]. This is very beneficial for grid-connected systems, allowing a reduction in grid power consumption during peak hours (resulting in cost savings). The downside of this design, as shown in [25] and depicted in Figure 11, is that the capacity of commonly used batteries (such as lead acid and LiFePO4) degrades over time as a function of the number and depth of charge and discharge cycles the battery experiences. As peak shaving occurs, battery capacity is steadily degraded and service life reduced until battery replacement is required.

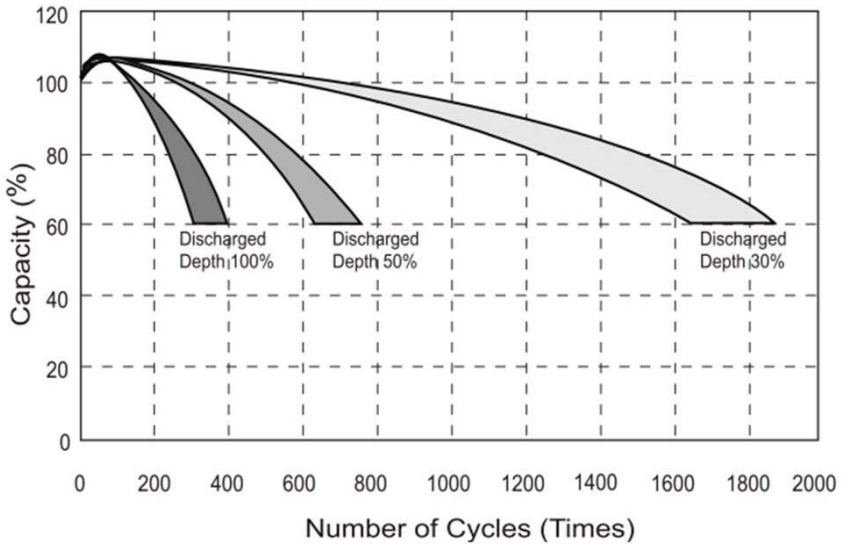

Figure 11. Battery Capacity Degradation as a Function of Discharge Depth and Number of Cycles. Source: [25].

By adding SC energy storage to form a HESS, the EMS can choose how much energy comes from the charged SC bank during load power peaks, removing these power cycles from the battery and extending battery life. This is done by using an LPF to separate the low frequency load changes from the high frequency load changes (power

peaks) and using these signals to schedule the amount of power coming from each HESS energy storage bank at any given time. A detailed description of the operation of the LPF is provided in Chapter III.A.5.

b. Removal of 120-Hz Ripple from Battery Bank Current

In addition to providing power during load power peaks, SCs can also be used to remove the second-order harmonic current ripple from the battery bank. The EMS makes use of a BPF to isolate the second-order harmonic ripple in DC link voltage and uses this signal to boost SC current output so that the SC bank acts as the source for this current ripple, removing it from the battery bank. This further extends battery life.

THIS PAGE INTENTIONALLY LEFT BLANK

III. MODELING AND SIMULATION

Modeling of the EMS system was completed using MATLAB and SIMULINK software. The individual systems that comprised this model, and how these systems were derived, are covered in this chapter.

A. EMS MODEL

There are many possible toolsets for simulating the EMS in SIMULINK. For the purpose of this thesis, it was determined that the simulation results could best be obtained by modeling the circuit using physics-based equations rather than by building the simulation with components from the SimPowerSystems block set, allowing for much shorter simulation times without sacrificing the accuracy of the results. This method of modeling the EMS ignores switching losses, switch turn-on and turn-off times, and assumes gate forward bias voltage = 0.0 V and that the system IGBTs are always gated with the duty cycle needed to achieve the desired current flow.

1. Top-Level System

The top-level system for the EMS simulation, shown in Figure 12, takes external inputs from the secondary controller and provides the necessary signals to the subsystems to control EMS operation. In order to tailor this simulation to the focus of this thesis (the effect of adding the SC bank with a LPF and a BPF), only the grid source connection status (Source ON and Source OFF) is provided as a secondary controller external input to the system.

The top-level system includes an option to "Turn on" the EMS by controlling the start time for current injection into the AC system when the grid source is connected and the EMS is operating as a constant current source. The major subsystems of this top-level system include a PWM subsystem for the H-bridge inverter, a Proportional Integral (PI) controller that takes several system inputs and produces a reference DC bus voltage v_{ref}, and the subsystem that models the physical system itself. This physical system includes a battery and SC HESS connected to the system loads via BBCs and the H-bridge inverter.

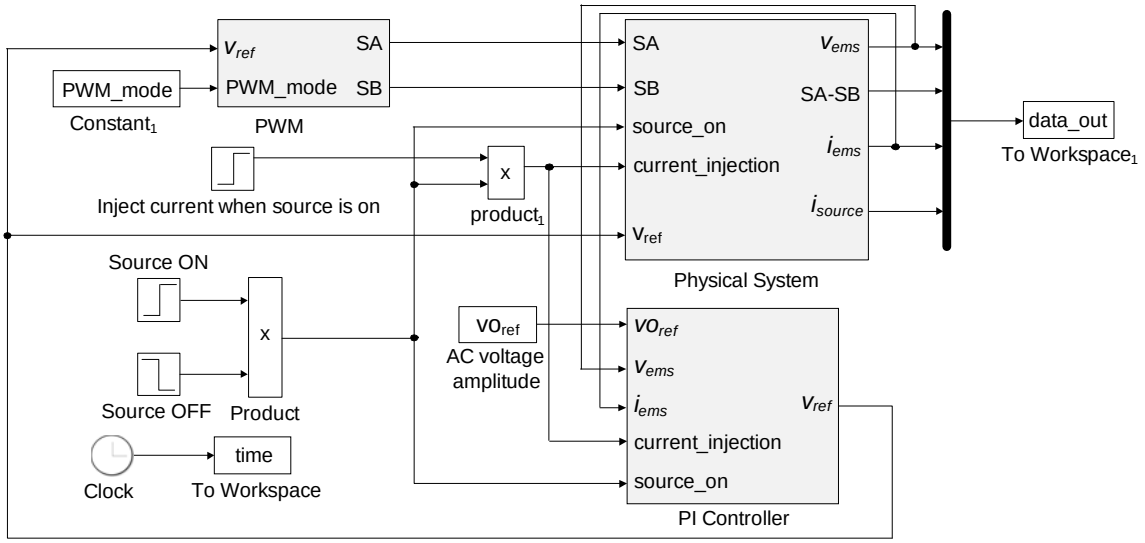

Figure 12. EMS Simulation Top-Level System

2. PWM System

The PWM subsystem, shown in Figure 13, uses a reference voltage v_{ref} from the output of the PI controller and a sine wave with the chosen H-bridge switching frequency to create two signals, SA and SB. These signals are provided to the physical system, where SA and negative SB are summed to provide a pulse-width modulated signal at the switching frequency with a peak-to-peak amplitude of two.

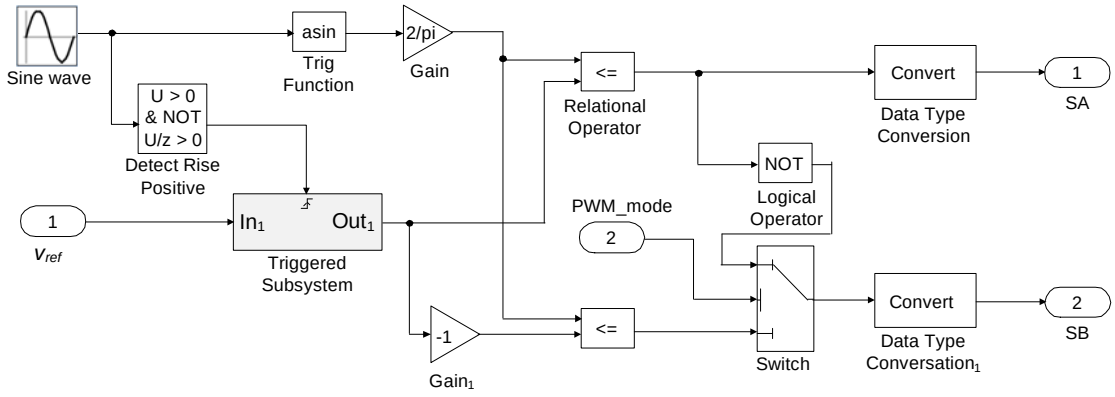

Figure 13. EMS Simulation PWM Subsystem

3. Physical System

The physical system simulates the operation of the portion of the EMS shown in Figure 14, which includes everything between the DC bus and the AC grid source.

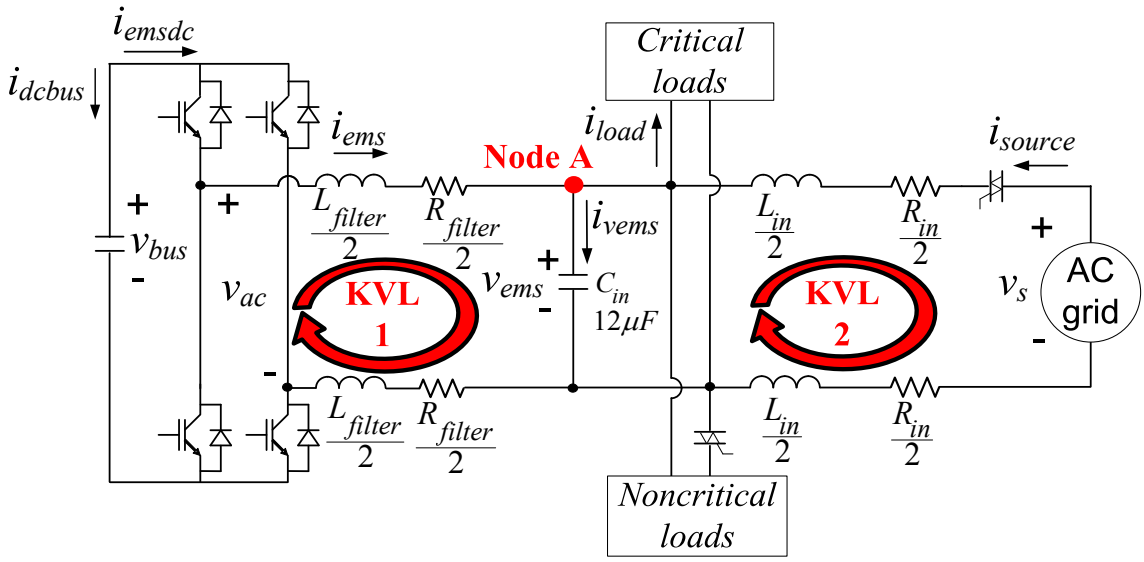

Figure 14. Physical System Schematic

Analysis of the physical system began with performing two Kirchhoff's Voltage Law (KVL) calculations (KVL 1 and KVL 2) and a Laplace domain Kirchhoff's Current Law (KCL) calculation at Node A to derive three equations. The first equation, obtained from KVL 1, is

$$v_{L_{filter}} = v_{ac} - v_{R_{filter}} - v_{ems} \ , \tag{7}$$

where $v_{Lfilter}$ is the voltage drop due to the EMS output filter inductance, $v_{Rfilter}$ is the voltage drop across the output filter resistance, and the other two terms (v_{ac} and v_{ems}) are as shown in Figure 14. The second equation, obtained from KVL 2, is

$$v_{L_{in}} = v_s - v_{R_{in}} - v_{ems} \ , \tag{8}$$

where v_{Lin} is the voltage drop across the input inductance and v_{Rin} is the voltage drop across the input resistance. The third equation, obtained from performing KCL at Node A, is

$$C_{in} s v_{ems} = i_{ems} + i_{source} - i_{load} \ , \tag{9}$$

where C_{in} is the input capacitance seen by the source, s is the Laplace domain derivative operator, and the two other terms (i_{ems} and i_{load}) are as shown in Figure 14. These three equations were used to build the SIMULINK model equivalent for Figure 14, as shown in Figure 15.

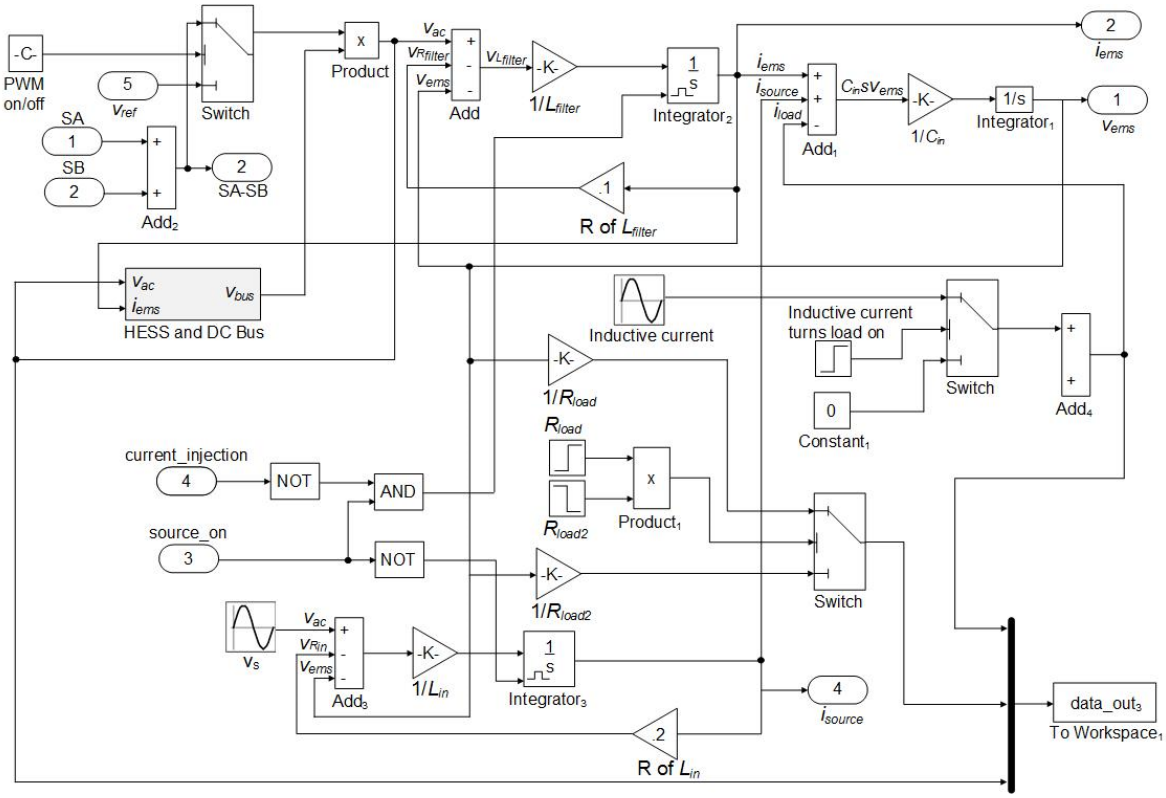

Figure 15. EMS Simulation Physical System

The pulse-width modulated AC voltage output of the H-bridge inverter is simulated directly without the need to generate H-bridge gate signals by subtracting SB from SA (both were retrieved from the PWM subsystem) and performing a multiplication with the DC bus voltage v_{bus} to produce v_{ac}. Using Switch1, the simulation also affords the option of multiplying v_{ref} (an output of the PI controller) and (SA minus SB) directly, which has the effect of producing v_{ac} without simulating the pulse-width modulation of the H-bridge inverter. This method of producing v_{ac} does not affect the simulation output but allows a larger simulation time-step size and, therefore, shorter overall simulation times. This method was used extensively for this thesis.

4. HESS and DC Bus System

This subsystem simulates the portions of the EMS shown in Figure 16, which includes the Battery and SC HESS and the BBCs that connect them to the DC bus. In order to maximize simulation speed, the individual switch modulation is not modeled. Instead, it is assumed that modulation takes place as necessary to achieve the desired boost currents (i_{boost} and $i_{scboost}$), which are set by the boost controller.

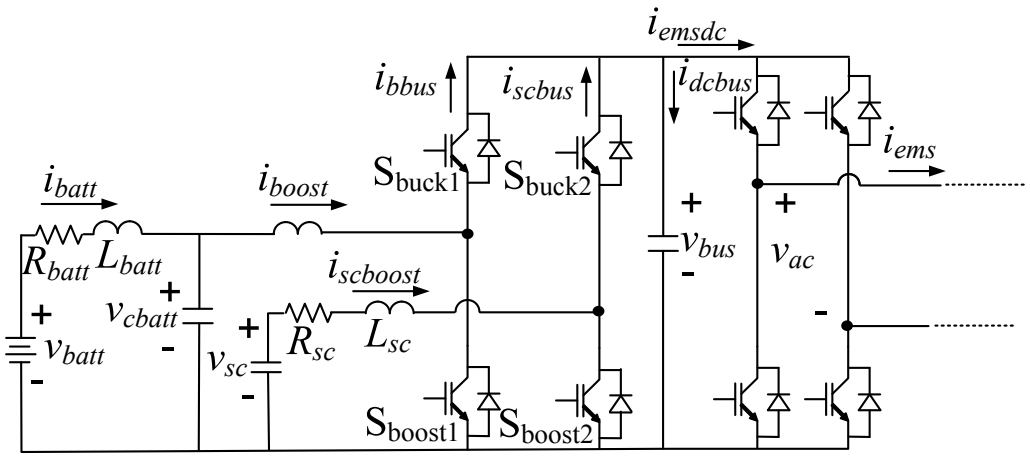

Figure 16. HESS and DC Bus System Schematic

The HESS SIMULINK model takes the EMS output current i_{ems} and voltage v_{ac} and employs a boost controller to derive the HESS boost currents necessary to maintain DC bus voltage v_{bus}.

a. Derivation of SC Boost Current ($i_{scboost}$) Model

To create the model for SC boost current $i_{scboost}$, Figure 16 was analyzed to derive the equations relating the desired HESS system current and voltage. The SC circuit schematic used to obtain the equations for $i_{scboost}$ is shown in Figure 17. The boost controller determines $i_{scboost}$, and the DC Bus Controller schedules the SC bank to provide $i_{scboost}$ to the DC bus by adjusting SC BBC IGBT gating.

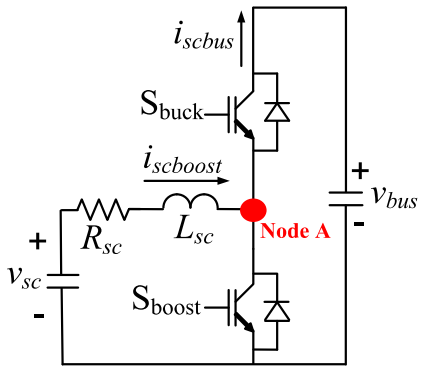

Figure 17. SC Converter Schematic

Using the power conservation law, $P_{in} = P_{out}$, we see that the power flow into Node A in Figure 17 must equal power out of the same node. Ignoring the small voltage drop across the SC ESR (8.1 mΩ) for the purposes of the simulation, we get

$$v_{sc} i_{scboost} = v_{bus} i_{scbus} \ , \tag{10}$$

where all terms are as shown in Figure 17. This equation can be rearranged to give the equation for SC boost current,

$$i_{scboost} = \frac{v_{bus} i_{scbus}}{v_{sc}} \ . \tag{11}$$

b. Derivation of Battery Boost Current (i_{boost}) Model

The battery bank circuit schematic used to obtain the equations for i_{boost} is shown in Figure 18. This current is determined by the boost controller and scheduled by the DC bus controller to be provided to the DC bus by the battery bank.

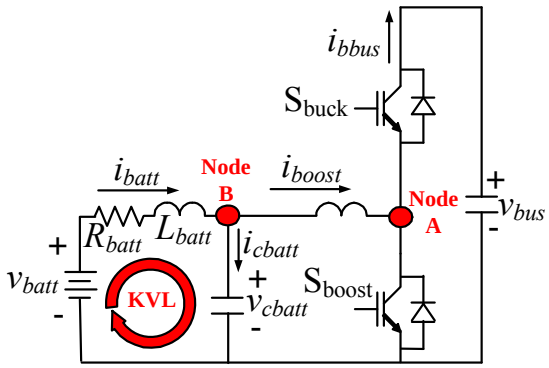

Figure 18. Battery Bank Converter Schematic

The derivation of i_{boost} involves the application of the power conservation law at Node A, KCL in the Laplace domain at Node B, and application of KVL as shown in Figure 18. The first equation, produced by a power conservation analysis at Node A, is

$$v_{cbatt} i_{boost} = v_{bus} i_{bbus} , \tag{12}$$

where all terms are as shown in Figure 18. The second equation, produced by performing KCL analysis at Node B, is

$$i_{batt} - i_{cbatt} = i_{boost} , \tag{13}$$

where all terms are as shown in Figure 18. The final equation, produced by performing a KVL, is

$$-v_{batt} + R_{batt} i_{batt} + Ls\left(i_{batt}\right) + v_{cbatt} = 0 , \tag{14}$$

where R_{batt} is the battery internal resistance, s is the Laplace domain derivative operator, and all other terms are as shown in Figure 18.

c. Derivation of DC Bus Current

In order to connect the simulation parameters on the HESS-side of the H-bridge inverter with those on the AC grid side, Figure 19 was analyzed to derive an equation for DC Bus current i_{dcbus}.

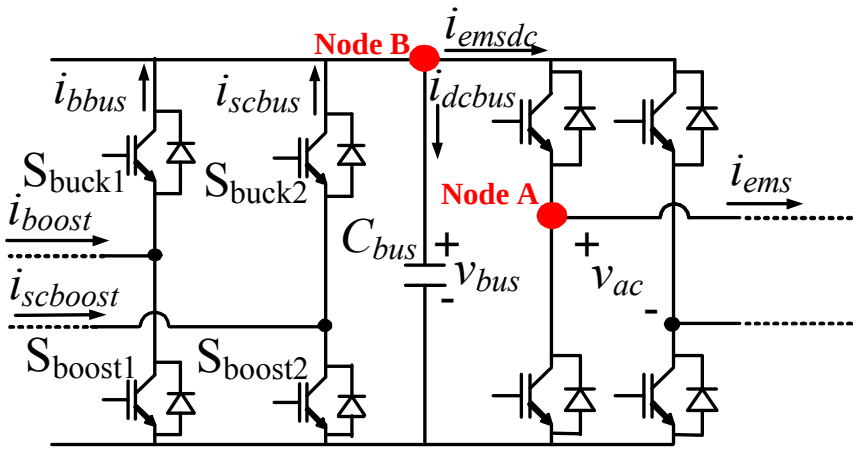

Figure 19. DC Bus Current Schematic

The derivation of an equation for i_{dcbus} involves the application of the power conservation law at Node A and the application of KCL in the Laplace domain at Node B. The power conservation law at Node A gives

$$v_{ac} i_{ems} = v_{bus} i_{emsdc} , \tag{15}$$

where all terms are as shown in Figure 19. The KCL analysis at Node B gives

$$i_{emsdc} = i_{bbus} + i_{scbus} - C_{bus} s v_{bus} , \tag{16}$$

where C_{bus} is DC bus capacitance and all other terms are as shown in Figure 19. Next, equations (15) and (16) were built into the SIMULINK model given in Figure 20.

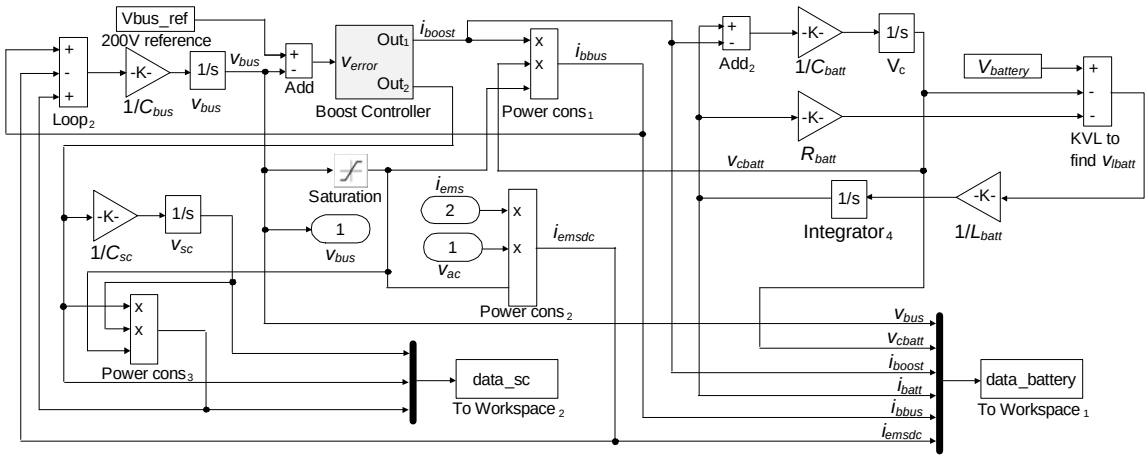

Figure 20. EMS Simulation HESS and DC Bus System

5. Configurable Boost Controller System

In order to extend battery bank life, it is desirable to provide current from the SC bank for all but the lowest (essentially DC) frequency v_{bus} changes and provide additional current from the SC bank to remove the second-order harmonic (120-Hz) current ripple from the battery bank. The SIMULINK model of a configurable boost controller that receives a DC bus voltage error (the difference between v_{bus} and the 200 V vbus_ref), sends it through a PI controller, and determines the battery bus boost current i_{boost} necessary to drive voltage error toward zero to maintain v_{bus} at 200 V in steady state is shown in Figure 21. To allow the introduction of a BPF and LPF into the system during simulations, the boost controller was designed to allow easy switching between three

different operating modes by adjusting the value of two constants in the model MATLAB script provided in Appendix A, "LPF_connection_status" and "SC_connection_status." The three operating modes are:

1. SC bank disconnected
2. SC bank connected with 120-Hz BPF only
3. SC bank connected with 120-Hz BPF and LPF.

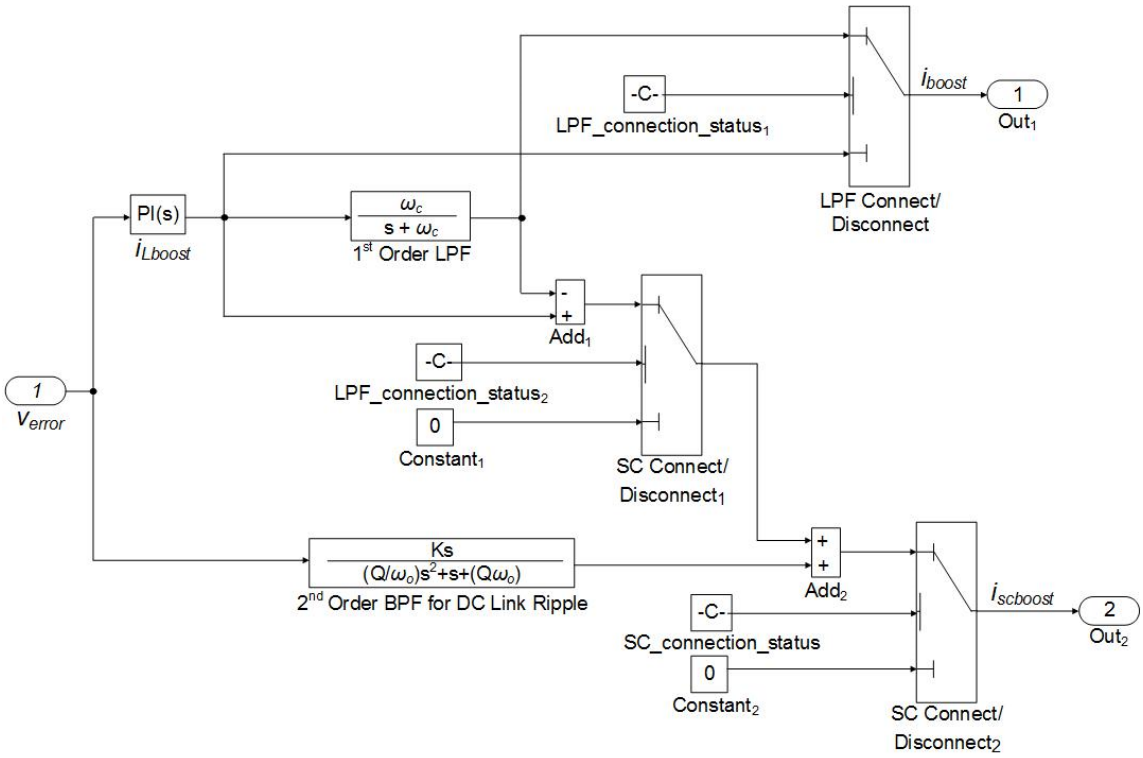

Figure 21. EMS Simulation Configurable Boost Controller

The boost controller LPF Laplace domain transfer function *T(s)*, which defines the relationship between the filter output voltage and the filter input voltage as a function of the input signal frequency, is given by [26]

$$T(s) = \frac{\omega_c}{s + \omega_c} \quad , \tag{17}$$

where $s = j\omega$ (the square-root of negative one times frequency in radians per second) and ω_c is the filter cutoff frequency in radians per second. For all simulations that employ the

LPF, ω_c = 0.1 rad/s, ensuring that only the lowest frequency load signals are used to create the battery boost current signal. The boost controller BPF Laplace domain transfer function is given [26]

$$T(s) = \frac{Ks}{\left(\frac{Q}{\omega_0}\right)s^2 + s + \left(Q\omega_0\right)}, \tag{18}$$

where K is the filter gain at mid-band, ω_o is the filter center frequency in radians per second (240π Hz), and Q is the filter Q-factor (center frequency divided by 3-dB bandwidth), which defines the width of the filter passband. The simulations in this thesis employ an active BPF with a gain K of 30, chosen to be greater than 1.0 to maximize the removal of the second order harmonic ripple from the battery bank and a Q-factor Q = 10 to allow for a reasonably narrow passband.

The boost converter provides two output signals to the HESS and DC Bus subsystem, i_{boost} and $i_{scboost}$. The DC bus voltage error is driven toward zero by the i_{boost} current coming from the battery bus, and $i_{scboost}$ is used to control the amount of load that the SC bank takes off of the battery bank (to include the current ripple caused by 120-Hz DC link ripple). For the simulations in this thesis, the i_{boost} and $i_{scboost}$ signals are driven directly by the output of the boost controller such that their value always exactly matches the commanded signals from the controller. This allows for much faster simulations without sacrificing the accuracy of results. For laboratory experimentation, by contrast, these two boost current signals are sent to the DC bus controller to modulate the BBC switches in order to achieve the desired i_{boost} and $i_{scboost}$ values.

Please note that all boost controller figures in this section depict switches in the positions associated with the applicable configuration, with wires and components greyed out when they are not being used.

a. SC Bank Disconnected

Simulations were performed with the SC bank disconnected to show the worst-case battery current ripple that is present during EMS operation when the battery bank is the only available energy source. In this operating mode, no filters are used. The output

of the PI controller directly sets the value of i_{boost}, and $i_{scboost}$ is set to a constant 0.0 A (effectively removing the SC bank from the system). When configured for this mode of operation, the boost controller schematic is as shown in Figure 22.

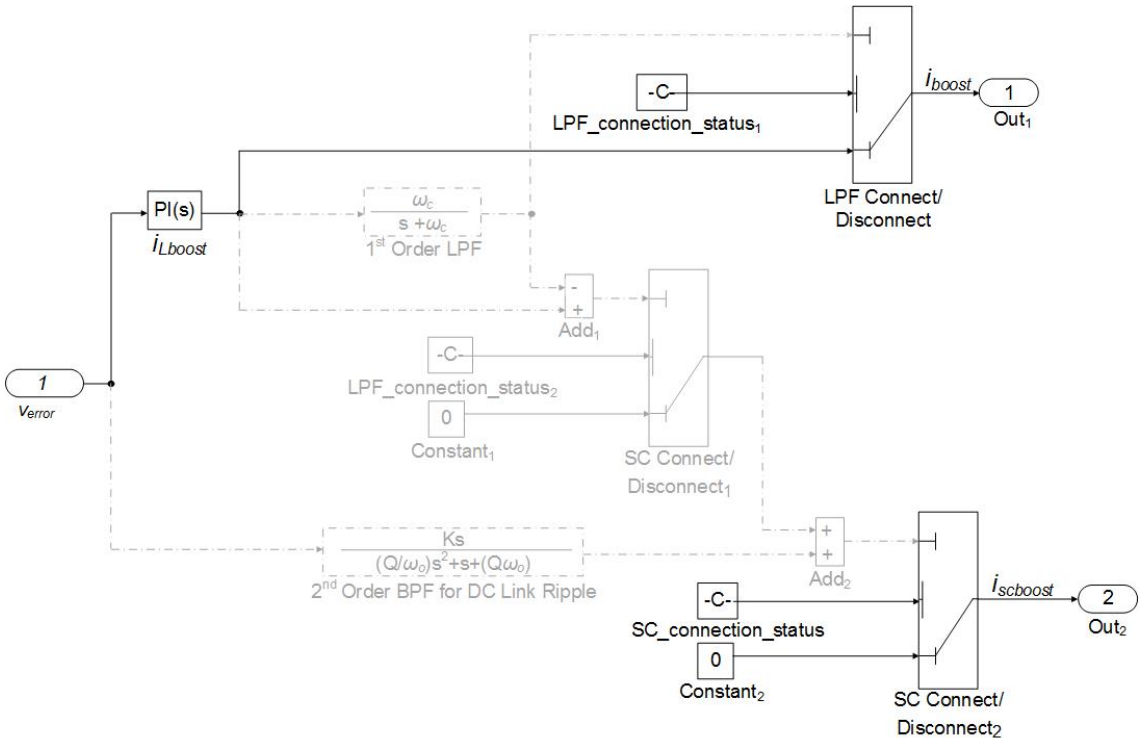

Figure 22. EMS Simulation Configurable Boost Controller– SC Bank Disconnected

b. SC Bank Connected with 120-Hz BPF Only

To show the benefits of adding the SC bank to the system, the boost controller is configured to send the input voltage error signal v_{error} through a 120-Hz BPF, the output of which is used to create the $i_{scboost}$ signal. The $i_{scboost}$ signal adjusts the current coming out of the SC bank in order to remove the 120-Hz ripple current from the battery and place the load requirement on the SC bank. While this configuration removes much of the 120-Hz current ripple from the battery bank, it allows all other current ripple frequencies (such as those that are encountered during a step change in load) to remain on the battery. This boost controller configuration is depicted in Figure 23.

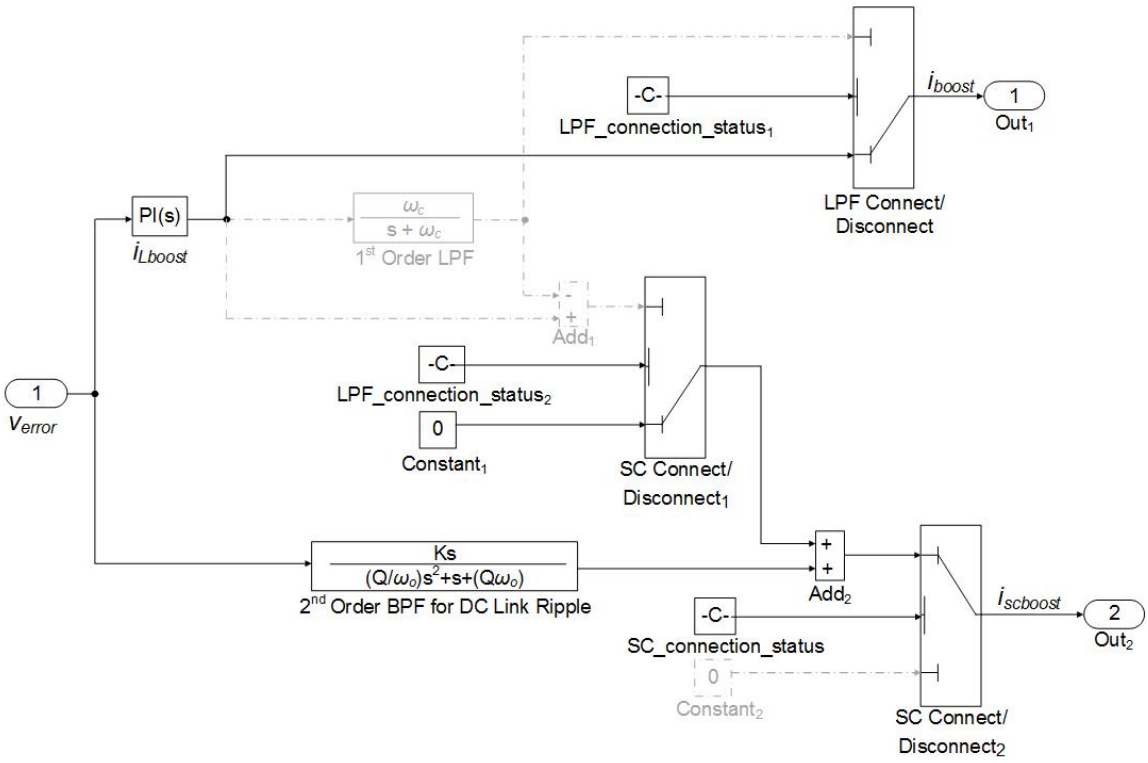

Figure 23. EMS Simulation Configurable Boost Controller–
SC Bank Connected with BPF

c. SC Bank Connected with 120-Hz BPF and LPF

While the 120-Hz ripple in battery current is greatly reduced by the addition of the SC bank with the BPF, adding a LPF on the output of the PI controller with a very low cutoff frequency ω_c is expected to reduce the 120-Hz current ripple to essentially 0.0 A and allow battery current to transition smoothly from its initial to final steady-state value when commanded battery current changes (such as during a load change). As shown in Figure 24, where the boost controller is configured with the SC connected and both a BPF and LPF employed, the signal prior to the LPF must be added to the output of the BPF and the signal after the LPF must be subtracted from the output of the BPF in order to ensure that all of the error signal that was removed from the i_{boost} signal is used to increase $i_{scboost}$. This allows the SC bank to remove as much of the 120-Hz ripple from the battery bank current as possible.

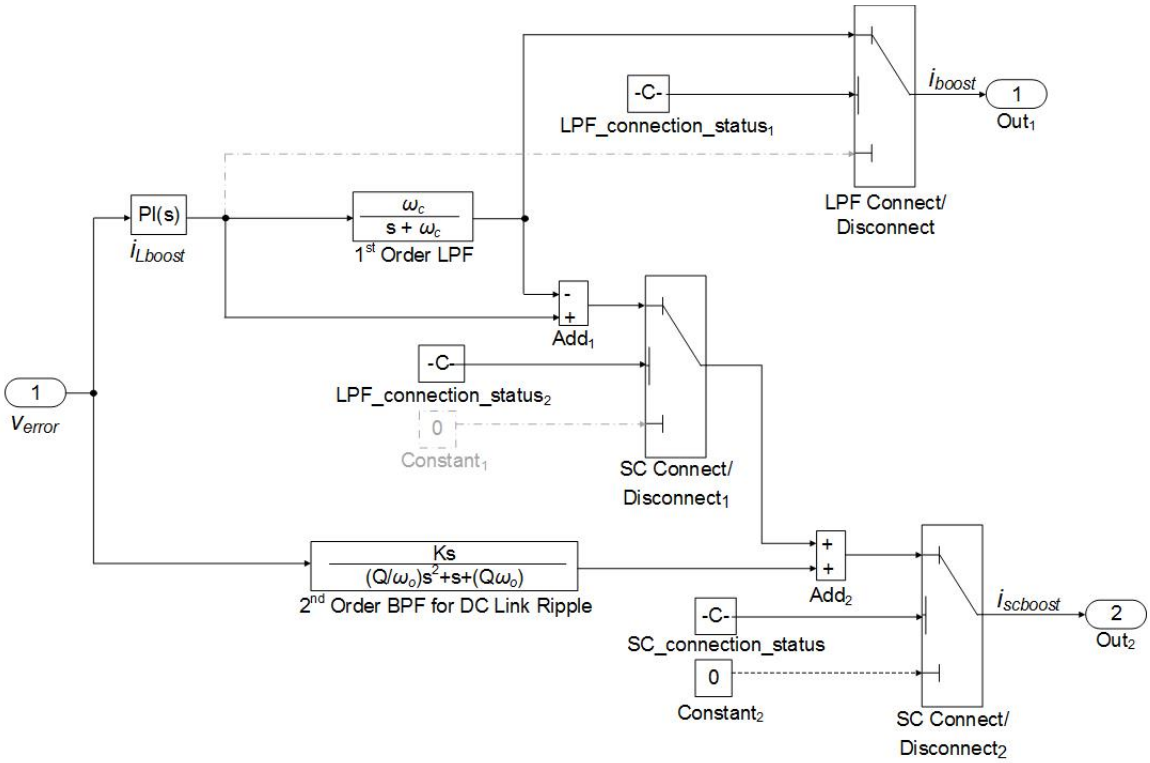

Figure 24. EMS Simulation Configurable Boost Controller– SC Bank Connected with BPF and LPF

B. SIMULATION FOR DIFFERENT LOAD AND SYSTEM CHARACTERISTICS

The simulations performed demonstrate the effect of using a battery and SC HESS on battery utilization, including the removal of the 120-Hz ripple from the battery bank current. To make these effects apparent, three SIMULINK models are compared under given load conditions: a model that includes a battery-only energy storage system (SC bank disconnected), a model that includes the battery and SC HESS with a 120-Hz BPF only, and a model that includes the battery and SC HESS with both a 120-Hz BPF and a LPF. These scenarios were modeled by changing the boost current controller as covered in the Configurable Boost Controller, Section A.5. For all scenarios, it is shown that the addition of the SC with BPF greatly reduces battery ripple current, and this ripple can be driven down further by the addition of a LPF. Additional measurements and calculations for both all simulations are provided in Appendix B.

1. Grid Connected, Operator Increases EMS Commanded Current

When the EMS is in "Grid Connected" mode, with the grid power source connected to the loads and EMS circuitry, the EMS operates as a constant current source. The EMS current is controlled by settings on the secondary controller, which an operator can change to meet desired conditions as the HESS and grid source share the load. In this scenario, at a simulation time of 10.0 s, a system operator provides input to the EMS primary controller to increase EMS output current i_{ems} from 1.0 A to 4.0 A. System load is set at 10.0 Ω for all three simulations below.

a. SC Bank Disconnected

With the SC bank disconnected, the battery bank has large peak-to-peak current ripples that increase as i_{ems} is increased, as shown in Figure 25.

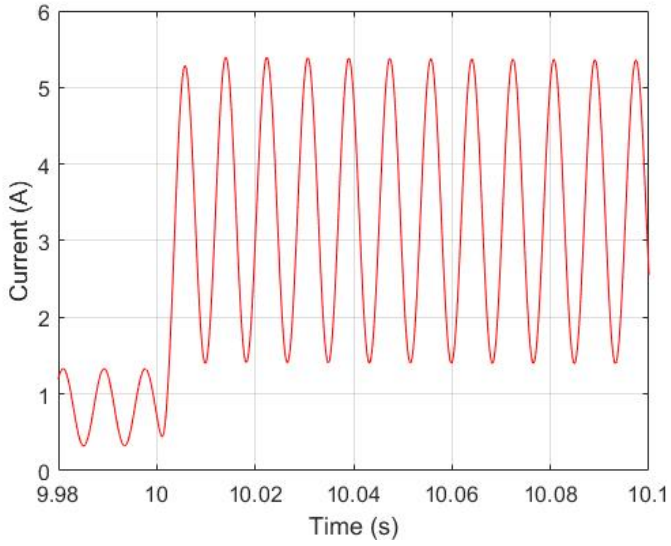

Figure 25. Battery Current, EMS Commanded Current Change– SC Bank Disconnected

The boost current controller senses DC bus voltage error (v_{bus}–v_{ref}) and controls battery boost current as required to maintain v_{bus} at 200 V. The 120-Hz ripple in v_{bus} causes a ripple in the generated $i_{scboost}$ signal, which transfers the current ripple to the battery bank. Battery peak-to-peak AC current ripple increases dramatically from 1.01

$A_{pk\text{-}pk}$ before the commanded current change to 3.95 $A_{pk\text{-}pk}$ after the step change that occurs at 10.0 s.

b. SC Bank Connected with 120-Hz BPF Only

In this configuration, the boost controller sends the DC bus voltage error through the 120-Hz BPF and uses this signal to adjust $i_{scboost}$ so that the SC bank provides the ripple current caused by the ripple in v_{bus} instead of the battery bank. As shown in Figure 26, the addition of the SC with a 120-Hz BPF greatly reduces the ripple in battery bank current i_{batt} both before and after the EMS commanded current change and also allows battery current to increase more slowly from the initial steady-state average value to the final steady-state value.

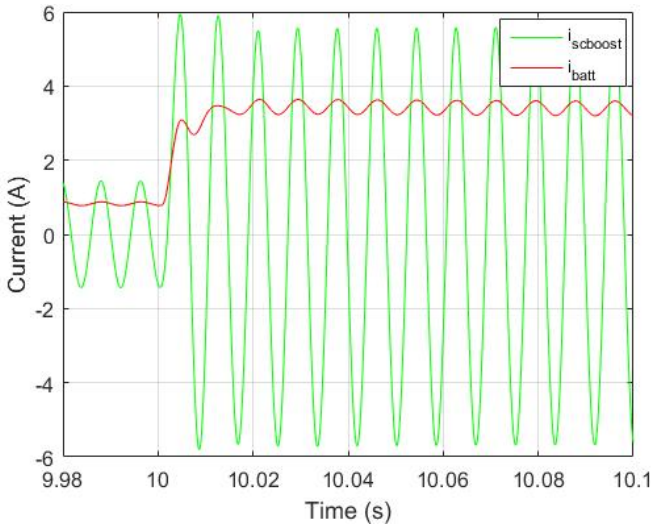

Figure 26. Battery and SC Current, EMS Commanded Current Change– SC Bank Connected with BPF

The battery bank peak-to-peak current ripple is reduced by approximately 89.90% at all points in the simulation when compared to the values obtained with the SC disconnected. From Figure 27, which is a close up view of the battery current after the commanded EMS output current change in Figure 26, it can be seen that the 120-Hz

ripple of 0.40 $mA_{pk\text{-}pk}$ is still present on the battery bank after the commanded EMS output current change despite the addition of the SC bank and BPF in the boost current controller.

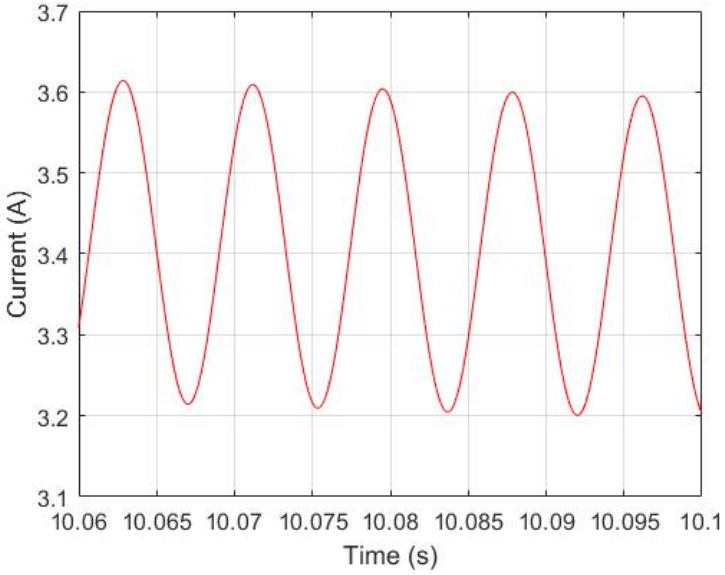

Figure 27. Battery Current 120-Hz Ripple, EMS Commanded Current Change– SC Bank Connected with BPF

c. SC Bank Connected with 120-Hz BPF and LPF

In this configuration, an LPF is added to the boost current controller to remove all but the lowest frequencies (the simulation uses 0.1 radians per second as the threshold frequency) from the battery boost current signal i_{boost} . Frequencies above the threshold are used to increase SC bank boost current $i_{scboost}$ and remove these higher frequency load requirements from the battery. As shown in Figure 28, the approximate steady-state average value of battery current before the commanded current change, 0.83 A, does not vary significantly from the value seen in Figure 26 with the system using a BPF only. Similarly, though not depicted in Figure 28 due to the fact that i_{batt} takes much longer (5.0 s) to reach steady state in this configuration, the steady-state average value of battery current after the commanded current change is also the same as in Figure 26 (3.40 A).

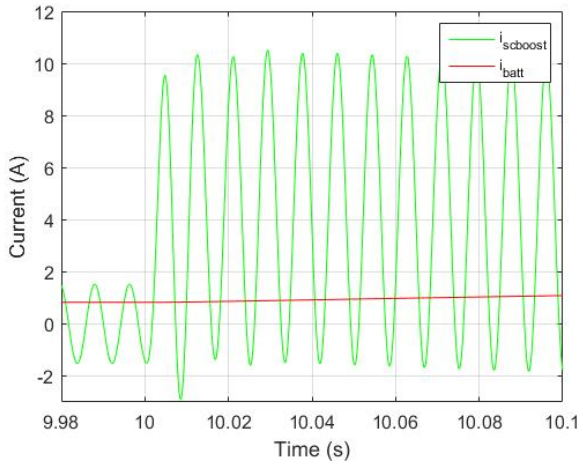

Figure 28. Battery and SC Current, EMS Commanded Current Change– SC Bank Connected with BPF and LPF

The peak-to-peak SC current increased from 3.05 $A_{pk\text{-}pk}$ to 11.92 $A_{pk\text{-}pk}$ due to the commanded current change, but the SC bank is well-suited to handle this larger peak-to-peak current, and this only represents an additional 0.49 $A_{pk\text{-}pk}$ increase in SC current ripple when compared with the "BPF only" scenario. This modest increase in peak-to-peak SC current allows the SC bank to remove an additional 10.06% of the 120-Hz battery bank ripple current, bringing the total removal to 99.99% when compared with the "SC Disconnected" scenario. A close-up view of the steady-state battery current after the change in EMS commanded current change is provided in Figure 29.

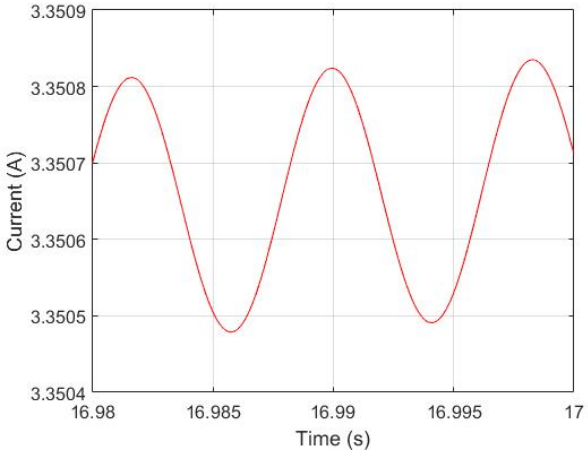

Figure 29. Battery Current 120-Hz Ripple, EMS Commanded Current Change– SC Bank Connected BPF and LPF

The advantage of adding the LPF to the boost controller circuitry is made clear in Figure 29. The 0.4 A_{pk-pk} 120-Hz ripple current that was previously seen on the battery after the commanded EMS output change has been reduced to 0.0003 A_{pk-pk}, which is essentially a complete removal of this ripple current.

2. Loss of AC Grid Source and Transition to Islanding Mode

Under normal conditions, the EMS operates in grid-connected mode with the grid providing most of the power for system loads. The power provided to the loads by the EMS is governed by the EMS current and peak-power shaving settings on the secondary controller, and the HESS stores the generated power from alternate power sources, such as a photovoltaic (PV) cell array, until needed. One of the many benefits of using an EMS with energy storage is the ability to continue providing power from the HESS to the system loads when the main grid power source is lost. With a battery-only energy storage system, the large transients that result from a sudden loss of grid cause fluctuations in battery bank current, quickly reducing battery stored energy and reducing battery life. When employing an SC bank with a BPF and LPF as part of a HESS, the high frequency components of the system currents can be shifted to the SC to extend battery life. The battery life extension afforded by the removal of the 120-Hz battery current ripple will prove particularly valuable if grid restoration is not possible in the near future since the length of time that the EMS can operate in islanding mode is extended and power for all system loads is provided without requiring a system shutdown for replacement of HESS batteries. In each of the three following simulations, the grid source is removed at a simulation time of 5.0 s, load is set at 10.0 Ω, and EMS reference current is 1.0 A.

a. SC Bank Disconnected

In this configuration, the loss of the AC grid at 5.0 s results in a drastic and almost immediate increase in battery ripple current from 1.01 A_{pk-pk} to 17.03 A_{pk-pk} in steady state, as shown in Figure 30. The large battery current fluctuations can greatly reduce battery life, and it is undesirable to operate on the batteries in this way for long periods of time.

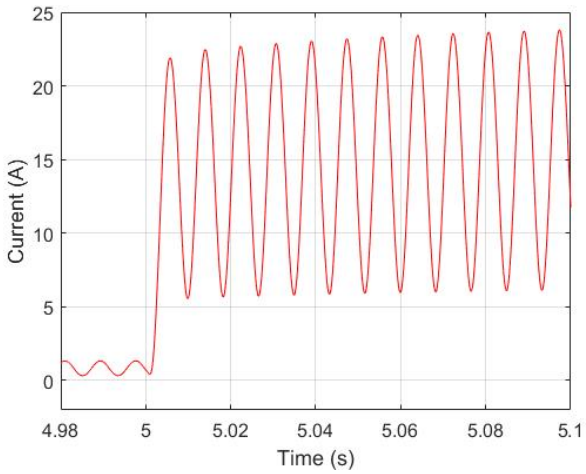

Figure 30. Battery Current, Loss of AC Grid Source–
SC Bank Disconnected

b. SC Bank Connected with 120-Hz BPF Only

As shown in Figure 31, the addition of the SC bank and BPF allows the SC to greatly reduce the battery current ripple as the AC source is lost. Average battery current increases from 0.83 A to its new steady-state value of 14.60 A during the 0.8 s following the loss of the AC grid. SC ripple current increases almost immediately from 2.88 $A_{pk\text{-}pk}$ to 49.48 $A_{pk\text{-}pk}$ to provide power for the increased load and continue removing the 120-Hz ripple from the battery current.

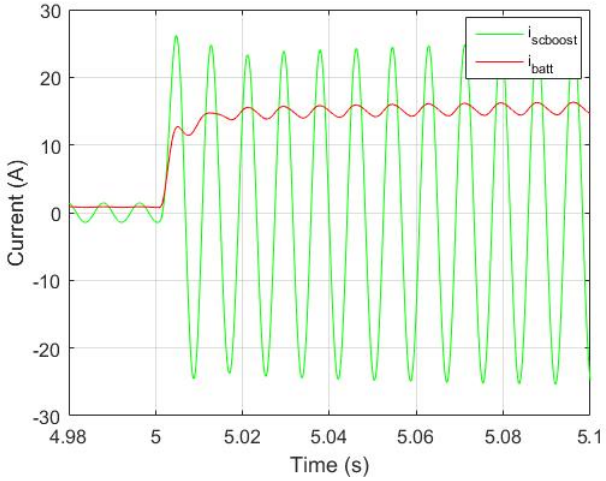

Figure 31. Battery and SC current, Loss of AC Grid Source–
SC Bank Connected with BPF

In Figure 32, which is a close-up view of the battery current in Figure 31, the 120-Hz current ripple of 1.76 $A_{pk\text{-}pk}$ (after loss of the AC grid source) can still be seen. This represents an 89.65% reduction in battery current ripple when compared with the "SC Disconnected" scenario, which is essentially the same reduction obtained by adding the SC with BPF in the "Grid Connected, Operator Increases EMS Commanded Current" simulation.

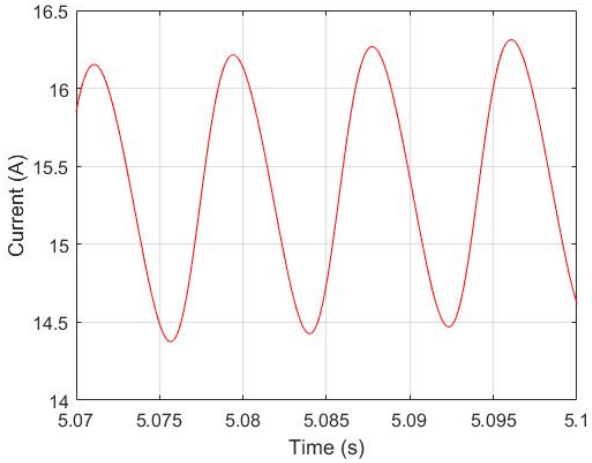

Figure 32. Battery Current 120-Hz Ripple, Loss of AC Grid Source–
SC Bank Connected with BPF

c. SC Bank Connected with 120-Hz BPF and LPF

Similar to the effect of adding the LPF in the "Grid Connected, Operator Increases EMS Commanded Current" simulation, the LPF removes all but the lowest frequency loads from the battery boost current signal i_{boost} and causes all other load frequencies to increase SC bank boost current $i_{scboost}$, removing these higher frequency load requirements from the battery. As shown in Figure 33, the approximate steady-state average value of battery current before the commanded current change, 0.82 A, does not vary significantly from the value seen in Figure 31 with the system using a BPF only. Similarly, though not depicted in Figure 33 due to the fact that i_{batt} takes much longer (10.0 s) to reach steady state in this configuration, the steady-state average value of battery current after the commanded current change is also the same as in Figure 31 (14.83 A).

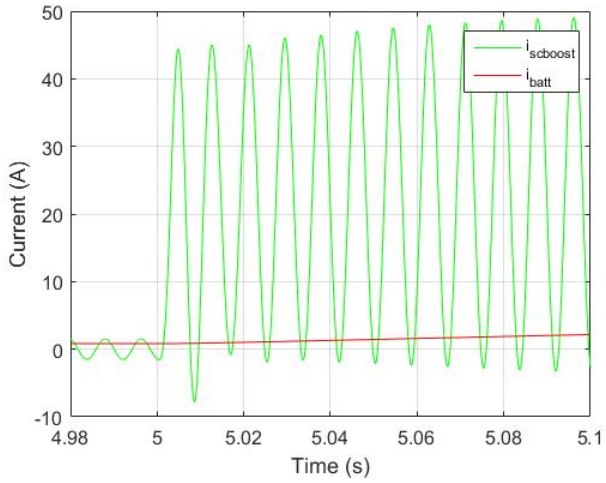

Figure 33. Battery and SC Current, Loss of AC Grid Source–
SC Bank Connected with BPF and LPF

As shown in Figure 33, the addition of the LPF increases SC current ripple from 3.04 $A_{pk\text{-}pk}$ to 52.14 $A_{pk\text{-}pk}$ following the loss of the AC grid source, which the SC and associated circuitry are well-suited to handle. This represents an additional 2.49 $A_{pk\text{-}pk}$ increase in SC current ripple when compared to the "BPF only" scenario but allows the removal of an additional 10.06% of the 120-Hz battery bank ripple current, bringing the total removal to 99.99% when compared to the "SC Disconnected" scenario. A close-up view of the final 0.001 $A_{pk\text{-}pk}$ battery current ripple is displayed in Figure 34.

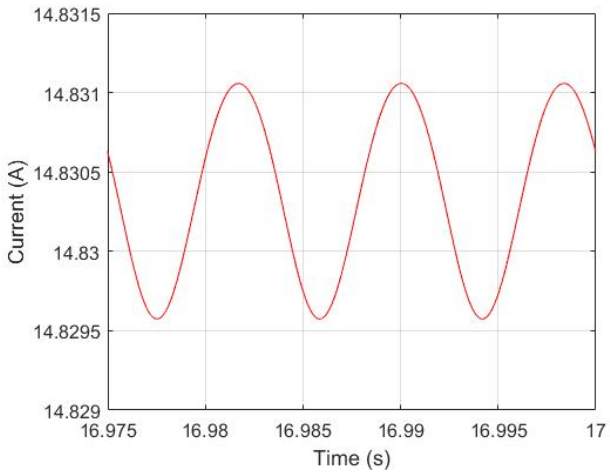

Figure 34. Battery Current 120-Hz Ripple, Loss of AC Grid Source–
SC Bank Connected with BPF and LPF

THIS PAGE INTENTIONALLY LEFT BLANK

IV. LABORATORY IMPLEMENTATION AND EXPERIMENTAL MEASUREMENTS

The focus of the laboratory experimentation for this thesis was to show that the SC bank of a HESS supplying a microgrid can be used to remove the 120-Hz ripple from the battery current, thereby extending battery life. It was decided that certain changes could be made to the system implementation used in simulation which would allow the system to be built using a single XILINX Field Programmable Gate Array (FPGA) while still providing confirmation 120-Hz current ripple removal from the battery bank. While the laboratory implementation described below is not an exact physical replication of simulations performed for this thesis, it is sufficient to show that SCs can be used to remove the 120-Hz current ripple from the battery bank. This experimentation methodology aims to mitigate the risk (cost and resources) of building a complete physical implementation of the simulated circuit and performing rigorous testing by performing limited testing that still validates system functionality.

A. DIFFERENCES BETWEEN SIMULATION AND PHYSICAL SYSTEM

The differences between the testing performed during simulation and the testing performed with the physical circuitry built in the laboratory are highlighted in this section. In each subsection below, a difference between the two test methodologies is identified and an explanation for why this difference does not affect the validity of laboratory analysis is provided.

1. Use of BPF Only

In simulations, a BPF was used to isolate the 120-Hz DC link ripple and use this ripple to increase the SC boost current, removing approximately 90% of the 120-Hz current ripple from the battery bank. A LPF was added to the boost controller and used to remove additional battery current ripple, bringing the total ripple current removal to 99.99% with the use of both filters. While this BPF with LPF configuration produced the largest reduction in battery ripple current, the parallel LPF and BPF circuitry (with associated feedback) is more difficult to build and program in the laboratory than a BPF

isolating only the 120-Hz ripple and using it to create the SC boost current. By using a BPF only, the reduction in battery ripple current that is possible with the addition of an SC bank can still be validated without the added difficulty of programming the additional LPF, so a LPF was not used for laboratory experimentation.

2. BPF Gain Reduced

The BPF gain K used for simulations was set at 30, which produced SC bank currents of up to 30.0 A in the laboratory. This current value is beyond the steady-state current-carrying capabilities of the FPGA and associated circuitry. As a result, the BPF gain was reduced to $K = 2$ so that useable results could be obtained without the possibility of overloading laboratory equipment.

3. SC Voltage Variation

For the purpose of simulation, it was necessary to assign the SC bank a starting voltage at the beginning of each simulation. While the value of this voltage affects the battery ripple current, it was decided that battery ripple current reduction could be achieved and demonstrated as long as each simulation used the same initial SC bank voltage. An arbitrary starting value of 56.0 V (the steady-state rated voltage limit of the 130.0 F Maxwell SC bank that was used in the laboratory) was chosen. Additionally, although the SC bank voltage is changing constantly during laboratory experimentation based on DC bus voltage and SC bank current, this voltage was held constant at 56.0 V during all simulations. This made it easier to focus the output plots on the effect of using the boost controller to control current drawn from the SC bank to reduce battery ripple current and was justified in that SC bank voltage is not expected to change significantly over the course of a short simulation (on the order of seconds). In laboratory experimentation, the SC bank voltage changed slightly over the course of each experiment, but the ability of the SC bank to provide the 120-Hz ripple current was still clearly visible.

4. Supercapacitor Current Monitored instead of Battery Current

Due to the EMS configuration in the laboratory and the space available for probe placement, it was more convenient to measure and display $i_{scboost}$ than i_{boost}. In order to provide a means of verifying that the 120-Hz current ripple was being removed from the battery bank by the addition of the SC bank and BPF, SC bank current was plotted with and without the use of a BPF. When using the BPF, the 120-Hz ripple that was removed from battery bank current was directly transferred to the SC bank, so demonstrating the appearance of this ripple in the SC bank current was sufficient to prove that the current ripple was removed from the battery bank.

5. Minimum Usable SC Bank Voltage

For all simulations, the commanded $i_{scboost}$ and i_{boost} currents derived by the boost controller were directly applied to the system without the simulation of BBC IGBT gating. This configuration ignored an important requirement placed on the physical system, as shown in [27], which is that the SC bank BBC must be maintained in Continuous Conduction Mode (CCM) in order to preserve the expected converter voltage transfer function

$$\frac{V_c}{E} = D\left(\frac{1}{1-D}\right), \tag{19}$$

where V_c is the voltage across the BBC output capacitor (v_{bus} capacitance), E is the BBC input voltage (SC bank voltage), and D is the IGBT duty cycle, or the percentage of each switching cycle during which the IGBT is off. The FPGA circuitry was programmed assuming that this transfer function was valid and is unable to properly maintain and control system parameters (such as $i_{scboost}$) if the transfer function were invalid. As the SC bank discharges to lower voltages, the BBC IGBT duty cycle increases to maintain $i_{scboost}$ equal to the boost controller commanded value until the BBC enters Discontinuous Conduction Mode (DCM) at some minimum usable SC bank voltage value. Once this minimum voltage value is reached, IGBT duty cycle increases are no longer able to maintain the commanded $i_{scboost}$ current. In practice, SC bank voltage dropped as low as approximately 5.0 V before the BBC entered DCM and data became invalid.

B. LABORATORY SETUP AND EQUIPMENT USED

The EMS was built in the laboratory and is depicted in Figure 35 with some of the major components labeled.

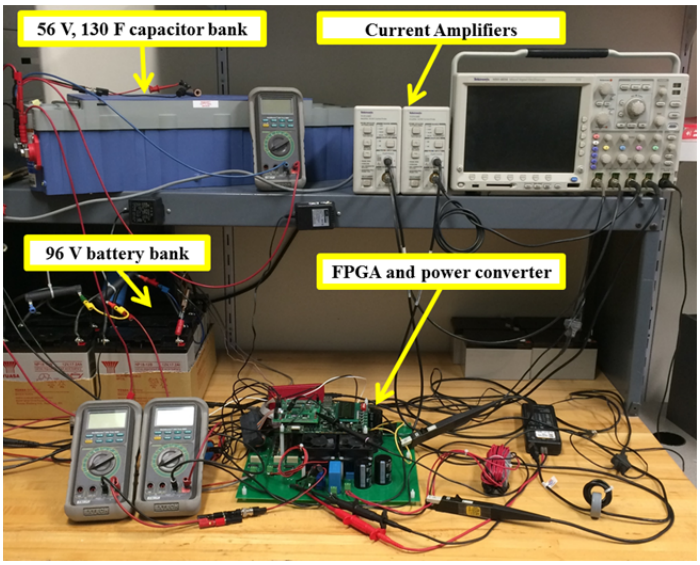

Figure 35. Laboratory Setup with Major Components Labeled

In addition to the major components depicted in Figure 35, the experiments also required a laptop with XILINX software installed to program and interface with the FPGA and a 200 V AC power supply (for grid simulation).

C. DIGITAL BPF DESIGN

The laboratory experimentation involved programming a XILINX FPGA to perform all of the functions of the EMS SIMULINK model. This code was written and provided by Naval Postgraduate School professor Alexander L. Julian, Ph.D. In simulations, the continuous-time Laplace domain transfer function for the 120-Hz BPF, given in (18), was used. The first task in designing the equivalent digital 120-Hz BPF for programming into the FPGA was to convert (18) into a discrete-time z-domain difference equation. In the MATLAB script provided in Appendix A, the bilinear transform function of MATLAB was first used to find the coefficients of the second-order BPF z-domain transfer function, producing

$$\frac{Y(z)}{X(z)} = \frac{z^2(0.1125) + z(0.0000) + (-0.1125)}{z^2(1.0000) + z(-1.9868) + (0.9925)}, \tag{20}$$

where *Y(z)* is the filter output, *X(z)* is the filter input, and

$$z = e^{j2\pi\left(\frac{f}{fs}\right)}, \tag{21}$$

where f is operating frequency and f_s is sampling frequency. A sampling frequency of 10.0 kHz was chosen. Rearranging (20) into the z-domain, BPF difference equation produces

$$Y(z) = (0.1125)X(z) + z^{-2}(-0.1125)X(z) - z^{-1}(-1.9868)Y(z) - z^{-2}(0.9925)Y(z). \tag{22}$$

To verify that (22) defines the operation of a 120-Hz digital BPF with the desired frequency response, the MATLAB script in Appendix A was plotted. From Figure 36, it can be seen that 120-Hz is in the center of filter pass band.

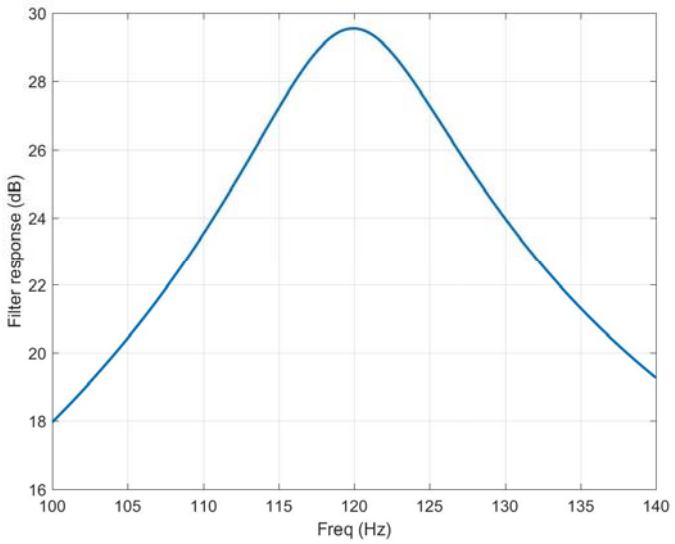

Figure 36. Digital 120-Hz BPF Response

By inspecting (22), we can see that the equivalent digital circuit for the desired BPF can be built with digital multipliers, adders, subtractors, and delay modules. The equivalent digital 120-Hz BPF is as shown in Figure 37.

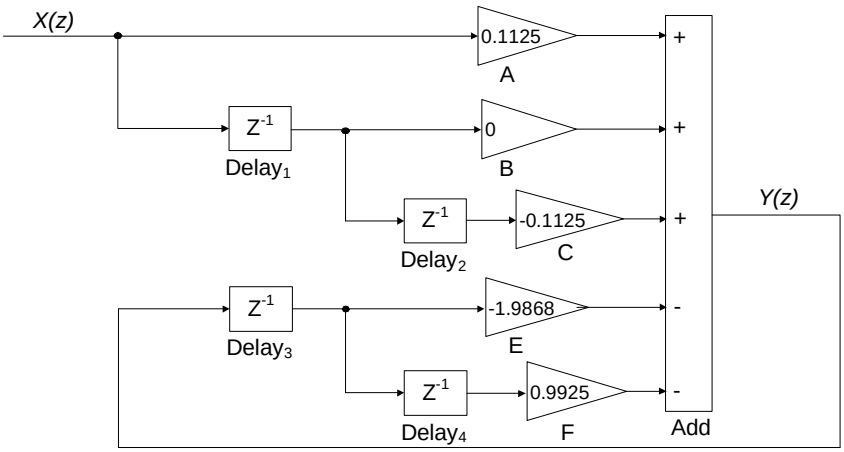

Figure 37. Equivalent Digital 120-Hz BPF

The SIMULINK model in Figure 37 was used to verify that (22) produced a true equivalent circuit to the desired 120-Hz analog BPF by passing a 120-Hz sine wave into both the analog and digital filter and plotting the output to produce Figure 38. The digital filter output is shifted downward by 0.001 in Figure 38 so that both waveforms are visible, but the output waveforms are otherwise exactly the same (as expected).

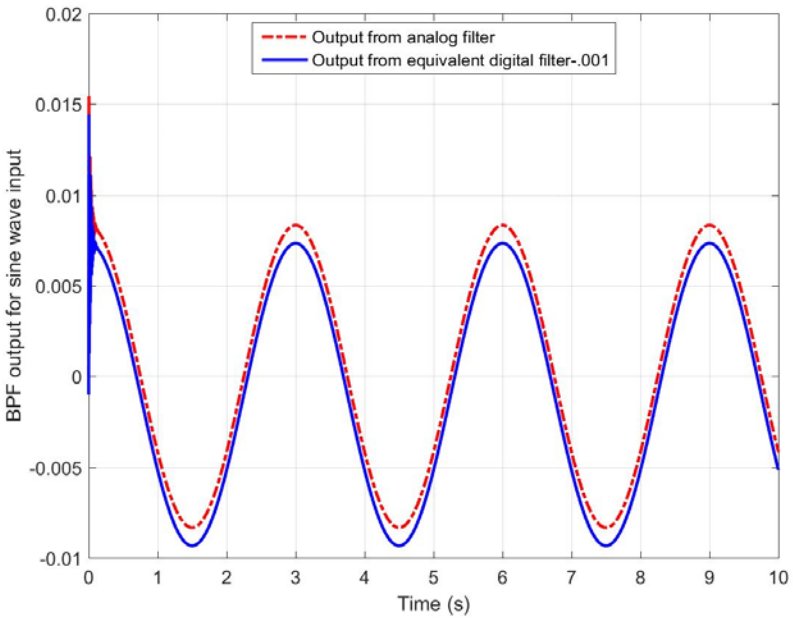

Figure 38. BPF Output For Sine Wave Input, Analog and Equivalent Digital Filter

D. LABORATORY TESTING AND RESULTS

The EMS DC bus controller was programmed to maintain the SC bank current at a constant 3.0 A (charging or discharging) when the BPF was not being employed to allow the removal of battery bank 120-Hz ripple current. SC charging and discharging operations were conducted both with and without the BPF, and source voltage v_s was plotted with SC current $i_{scboost}$ in each case. All experiments were performed (and plots captured) with the SC bank voltage at 14.0 V.

1. SC Charging

When in charging mode, the SC bank BBC operates as a buck converter in CCM. Current flowing into the SC bank during a charge is arbitrarily defined as the negative direction of current, based on current sensor placement. The EMS was placed in charging mode, increasing SC bank voltage from an initial 0.0 V to 14.0 V, at which point v_s and $i_{scboost}$ were recorded. Without the BPF, v_s and $i_{scboost}$ are as plotted in Figure 39. As expected, average SC bank current is approximately –3.0 A (with a slight offset due to a small amount of sensor inaccuracy), and there is no 120-Hz ripple present in $i_{scboost}$.

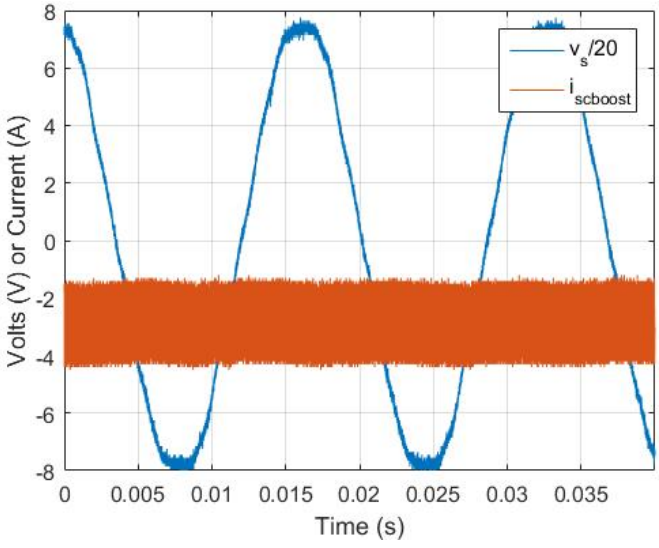

Figure 39. SC Charging, No BPF

A close-up view of the SC bank current in Figure 39 is provided in Figure 40. In this figure, it is clear that the SC bank current ripple in Figure 39 is caused by the combination of the 15-kHz IGBT switching frequency and duty cycle.

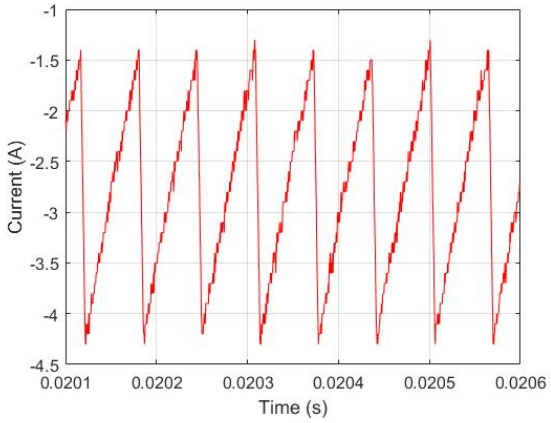

Figure 40. SC Current Ripple Caused By Duty Cycle and 15 kHz Switching Frequency

Connecting the BPF to the boost controller, the DC bus controller adjusts SC bank IGBT duty cycle to provide the $i_{scboost}$ current necessary to remove the 120-Hz ripple current from the battery bank. In this configuration, plots of v_s and $i_{scboost}$, shown in Figure 41, clearly demonstrate that the 120-Hz ripple was removed from the battery bank and placed on the SC bank. This ripple has an amplitude of approximately 3.1 $A_{pk\text{-}pk}$.

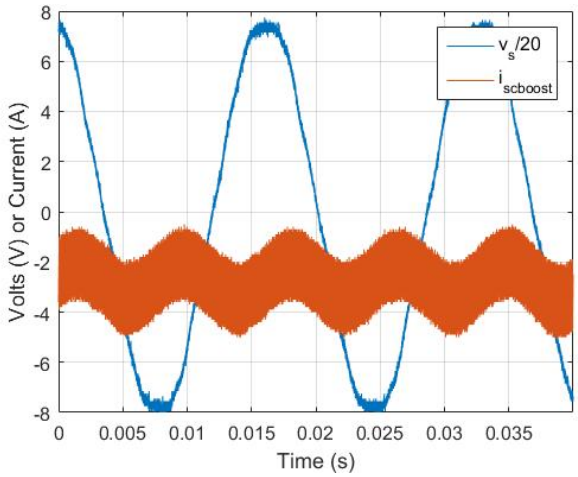

Figure 41. SC Charging, with BPF

2. SC Discharging

When in discharging mode, the SC bank BBC operates as a boost converter. Without the BPF, v_s and $i_{scboost}$ are as plotted in Figure 42. As expected, average SC bank current is approximately 3.0 A, and there is no 120-Hz ripple present in the SC bank current.

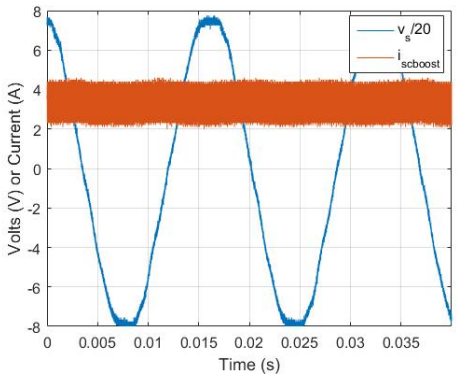

Figure 42. SC Discharging, No BPF

Similar to the results obtained during the "SC Charging" experiment, connecting the BPF to the boost controller causes the DC bus controller to adjust SC bank IGBT duty cycle to provide the $i_{scboost}$ current necessary to remove the 120-Hz ripple current from the battery bank. In this configuration, plots of v_s and $i_{scboost}$, shown in Figure 43, again demonstrate that the 120-Hz ripple was removed from the battery bank and placed on the SC bank. This ripple has an amplitude of approximately 2.3 $A_{pk\text{-}pk}$.

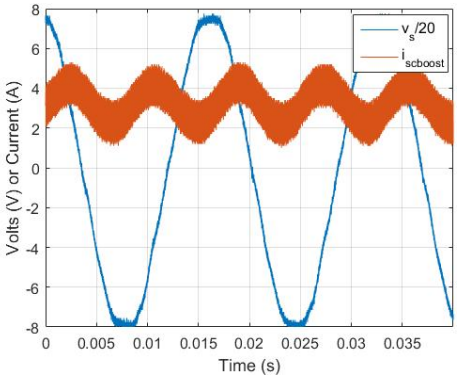

Figure 43. SC Discharging, with BPF

THIS PAGE INTENTIONALLY LEFT BLANK

V. CONCLUSIONS AND RECOMMENDATIONS FOR FUTURE WORK

The work conducted throughout this thesis provides many interesting conclusions, as well as room for potential follow-on research and experimentation. In this section, some of the more pertinent results are detailed in the sincere hope that future students and researchers will pick up the mantle and continue to develop this system into a useable end-product, delivering concrete benefits for our Armed Forces and the power industry.

A. CONCLUSIONS

The primary research objective of this thesis was to show through both simulation and laboratory experimentation that when using an EMS on a microgrid with a single-phase VSI, the battery bank ripple current caused by the second-order harmonic DC link voltage ripple can be filtered out by adding an SC bank to the system with a BPF and boost controller circuitry. In the accomplishment of this objective, several specific conclusions were uncovered.

1. The Benefits of Employing an EMS Are Clear

The simulations and laboratory experimentation performed for this thesis have clearly shown that an EMS can be programmed to control the operation and utilization of DR, allowing different power sources and energy storage methods to provide services to a microgrid in ways that are not possible without an EMS. Specifically, the characteristics of power flow to and from different HESS energy storage devices can be individually controlled so that each device operates more efficiently. This is especially important when dealing with batteries as an energy storage method, since unnecessary cycling caused by harmonic ripples in DC bus voltage can quickly degrade battery capacity and lead to increased energy costs when battery banks require replacement. Additionally, simulations confirmed that the microgrid is able to increase power system redundancy by maintaining a stable power supply to system loads when the grid source is lost, which is highly desirable for systems powering vital loads. The optimization of microgrid parameters is achieved without any negative effect or need for control of the

grid source, making the microgrid an excellent control method for portable systems requiring a stable, redundant power source.

2. SCs Can Be Used to Remove Battery Bank 120-Hz Current Ripple

The ability to remove the battery bank 120-Hz current ripple by adding an SC bank with a BPF and boost controller was clearly demonstrated in this thesis. In two separate simulation scenarios, this additional system was shown to reduce battery bank ripple current by almost 90% when compared to operations without the SC bank and BPF. In laboratory experimentation, the SC bank current was measured to confirm that the 120-Hz current ripple was removed from the battery bank as desired. Even at the relatively low loading and current values achievable in the laboratory (based on system component limitations) the removal of more than 3.0 $A_{pk\text{-}pk}$ of ripple current from the battery bank was demonstrated. While not explored in this thesis due to time constraints, it can be inferred that this control methodology can be extended to other harmonics of concern in microgrids employing slightly different architectures (such as three-phase AC source systems).

3. Almost 100% of Battery Bank 120-Hz Current Ripple Can Be Removed with a BPF and a LPF

As a secondary research objective, the possibility of further reducing battery bank ripple current by adding an LPF to the boost controller was explored in this thesis. Two different simulations provided confirmation that a battery ripple current reduction of up to 99.99% is achievable when the LPF is added to the EMS and properly tuned as compared to a system employing a battery bank as the only energy storage method. This relatively simple addition to the boost controller functionality enables the system designers to achieve an almost complete removal of second-order harmonic ripple current from the battery bank, bringing the system close to maximum efficiency.

B. RECOMMENDATIONS FOR FUTURE WORK

As with any research endeavor, while working toward the research objectives for this thesis, the topics explored raised questions and brought to light opportunities for

future work. One of the many benefits of working with the EMS in simulations and in the laboratory is that there is both an endless universe of possible expansion areas for this research and a great need for this expansion. As stated in the introduction, energy costs are an enormous burden throughout the DOD; anything that can be done to reduce these costs will have a direct positive impact on our nation. The recommendations for future work focus on moving closer to translating the current system into a useable end-product

1. Test with a Higher Voltage Capacity SC Bank and More Robust EMS

The laboratory experimentation for this thesis was limited by the size of the SC bank and the voltage and current limitations of EMS circuitry. For example, it was not possible to increase the battery current to values large enough to allow the observation of the 120-Hz ripple current, although it was clearly shown to exist. Using an SC bank with a higher voltage capacity allows for more robust experimentation, such as the physical implementation of the two simulations performed in this thesis and longer experiments (due to the larger SC energy storage capacity).

2. Add Other Power Sources, such as PV Cells

Adding PV cells to the proposed EMS configuration would provide yet another means by which system efficiency can be optimized. With the increasing prevalence of solar systems used as alternative sources of energy, it would be prudent to explore how a PV cell could best be integrated into this system.

3. Optimize SC Bank Efficiency

While SCs are capable of operating through many more cycles than a typical battery before requiring replacement, their life is also decreased when the battery bank current ripple is shifted to the SC bank. In [28], Abeywardana et al. explore a current-feedback method that reduces SC bank harmonic ripple current to optimize SC bank life. The work performed in this thesis can be expanded to include this method or another means of reducing SC bank current ripple to maximize overall system efficiency and cost-effectiveness.

THIS PAGE INTENTIONALLY LEFT BLANK

APPENDIX A. MATLAB SCRIPTS

```
%% LCDR Gabriel Hernandez, Thesis
% With assistance from:
% NPS Prof. Giovanna Oriti
% NPS Prof. Alexander Julian
% NPS Prof. Roberto Cristi
%
% Create input values for SIMULINK model

clear all;
close all;

%%  Establish variable values
Kp_v = .00005;
Ki_v = .05;
sw_freq = 15000;
vo_ref = 120*sqrt(2)*2/pi;
vbus_ref = 200;  % Reference DC bus voltage
Lin = 400e-6;  % Includes the leakage inductance of the 60Hz xfmr,
which is 3mH
Lfilter = (470+470+220)*1e-6;  % Includes the leakage inductance of the
60Hz xfmr, which is 3mH
Cin = 12e-6;
PWM_mode = 1;
Vbattery = 100;
Lbattery = 100e-6;
Rbattery = .1;
Cbattery = 1000e-6;
Cbus = 1000e-6;
Lpv = 5000e-6;
Cpv = 4000e-6;
delta_I = .1;
deltav = .004975;
Isc = 4;
Rp = 1;
Rs = .05;
Io = 1e-10;

%% PV cell calculations

Vd = zeros(1,122);
IPV = zeros(1,122);
VPV = zeros(1,122);
Vd(1) = .02;
IPV(1) = Isc-Io*(exp(38.9*Vd(1))-1)-Vd(1)/Rp;
VPV(1) = Vd(1)-IPV(1)*deltav;
for ii = 2:122
    Vd(ii) = Vd(ii-1)+deltav;
    IPV(ii) = Isc-Io*(exp(38.9*Vd(ii))-1)-Vd(ii)/Rp;
    VPV(ii) = Vd(ii)-IPV(ii)*deltav;
end
for ii = 1:122
```

```
    IPV_rev(ii) = IPV(123-ii);
    VPV_rev(ii) = VPV(123-ii);
end
IPV_LU = [1:122]/122*4;
VPV_LU = [1:122]*0;
IPV_LUindex = [1:122];
nn = 2;
for ii = 1:121
    while IPV_rev(nn)<IPV_LU(ii)
        nn = nn+1;
    end
    slope = (VPV_rev(nn)-VPV_rev(nn-1))/(IPV_rev(nn)-IPV_rev(nn-1));
    VPV_LU(ii) = slope*(IPV_LU(ii)-IPV_rev(nn-1))+VPV_rev(nn-1);
end

Power_PV = VPV.*IPV;

%% Values most often adjusted

% Simulation start/stop and step times
pwm_on = 0;  %H bridge is PWM modulated when this variable is 1
tstop = 17;

if pwm_on == 0
      tstep = 15e-6;
else
     tstep = 10e-6;
end

% Turn source voltage on/off
source_on = 20;  % time when source connects
source_off = 25;  % time when source disconnects

% Added portion for supercapacitor
vsc = 56; % Voltage limit of supercapacitor is 56V. In laboratory, will
start from complete discharge
rsc = 8.1e-3;
lsc = 1000e-6;
csc = 130;
sc_connection_status = 1; %"1" = SC bank connected, "0" = SC bank
disconnected. BPF is connected with SC Bank
lpf_connection_status = 1; %"1" = LPF connected, "0" = LPF disconnected

% BPF for 120Hz oscillation
K = 30;
bpf_freq = 120;
bpf_wo = 2*pi*bpf_freq;
lpf_freq = .1;
lpf_wc = 2*pi*lpf_freq;
Q = 10;

% Allow for a load change during operation
Rload = 200;
Rload2 = 10;
```

```
Rload_applied = 0;
Rload2_applied = 5;

% Change EMS reference current
iref_change_at_time = 20;
iref_initial_value = 1;
iref_final_value = 4;

%% BPF Design

% Calculate BPF Z-transform coefficients using bilinear transformation
%   Gives the Z-domain transfer function required for the equivalent
%   digital filter to the analog filter governed by the chosen S-domain
%   transfer function
fs = 10e3; % Assume 10kHz sampling frequency
[numd,dend] = bilinear([(K) 0],[(Q/bpf_wo) 1 (Q*bpf_wo)],fs);

% Verification of BFP frequency response.

low_freq = 100; % Lowest plot frequency
high_freq = 140; % Highest plot frequency
points = 1000;
spacing = (high_freq - low_freq)/(points - 1); % Spacing between
frequencies

for i = 1:points
    freq_val(i) = low_freq + (i-1)*spacing;
    Z = exp(j * 2 * pi * freq_val(i) / fs); % The definition of Z
    H_z = ((Z^2)*numd(1) + Z*numd(2) + numd(3))/...
        ((Z^2)*dend(1) + Z*dend(2) + dend(3));
    mag(i) = abs(H_z);
    phase = angle(H_z)*180/pi;
end

% Plot BPF output
figure(12)
plot(freq_val,20*log10(mag));
xlabel('Freq (Hz)');
ylabel('Filter response (dB)')
set(gca,'FontSize',12)
grid on
print(gcf,'-dtiff','-r350','BPF output')
savefig('BPF Output')
```

```
%% LCDR Gabriel Hernandez, Thesis
% With assistance from:
% NPS Prof. Giovanna Oriti
% NPS Prof. Alexander Julian
% NPS Prof. Roberto Cristi
%
% Plot SIMULINK waveforms

close all

v_ems=data_out(:,1);
i_ems=data_out(:,3);
i_s=data_out(:,4);

i_ref=data_out2(:,1);
v_ref=data_out2(:,2); % Reference voltage when grid-connected

%% data_battery - Battery MUX output
v_bus=data_battery(:,1);
v_batterycap=data_battery(:,2);
i_boost=data_battery(:,3);
i_batt=data_battery(:,4);   % actual battery current
i_bus=data_battery(:,5);
i_emsdc=data_battery(:,6);   % into DC bus...called "ibus" in simulink
model

%% data_sc - SC MUX output
v_sc=data_sc(:,1);         % Voltage across sc
i_scboost=data_sc(:,2);       % Current in scbus
i_scbus=data_sc(:,3);     % supercapacitor boost current

%% data_out3 - MUX output from physical system
real_and_ind_iload=data_out3(:,1);
iload=(data_out3(:,2));
v_ac = (data_out3(:,3));
SC_power_out = v_sc.*i_scboost;
batt_power_out = v_batterycap.*i_boost;

t_ss=round(.1/tstep);
one_cycle=round(1/60/tstep);
vac_ss=v_ems(t_ss-2*one_cycle:t_ss-one_cycle);
vac_spect=fft(vac_ss)/(one_cycle/2);
freq_vac=[0:one_cycle]*60;
v_inv=data_out(:,2);

%% data_out4 - Boost controller transformation verification output

sine_in = data_out4(:,1);
analog_bpf_op = data_out4(:,2);
discrete_bpf_func_op = data_out4(:,3);
h_domain_built_bpf_op = data_out4(:,4);

% Verification plot for boost controller
```

```
figure(11)
plot(bpf_time,analog_bpf_op,'r-.')
hold on
xlabel('Time (s)')
ylabel('BPF output for sine wave input')
plot(bpf_time,h_domain_built_bpf_op-.001,'b')
leg11 = ...
    legend('Output from analog filter','Output from equivalent digital
filter-.001','location','best');
fig11_leg = findobj(leg11,'type','text');
set(fig11_leg,'FontSize',12)
set(gca,'FontSize',12)
grid on
hold off
print(gcf,'-dtiff','-r350','Boost Controller Verification')


%% Plot figures

%---------------%
figure(1);
%---------------%

plot(time,i_scboost,'g')
hold on
plot(time,i_batt,'r')
xlabel('Time (s)')
ylabel('Current (A)')
leg1 = legend('i_{scboost}','i_{batt}','location','best');
fig1_leg = findobj(leg1,'type','text');
set(fig1_leg,'FontSize',12)
set(gca,'FontSize',12)
grid on
print(gcf,'-dtiff','-r350','isc_boost and i_batt')
savefig('isc_boost and i_batt')

%---------------%
figure(2)
%---------------%

plot(time,v_bus,'b');
xlabel('Time (s)')
ylabel('v_{bus} (V)')
leg2 = legend('v_{bus}','location','best');
fig2_leg = findobj(leg2,'type','text');
set(fig2_leg,'FontSize',12)
set(gca,'FontSize',12)
grid on
print(gcf,'-dtiff','-r350','v_bus')
savefig('v_bus')
```

```
%---------------%
figure(3)
%---------------%

plot(time,i_batt,'r')
xlabel('Time (s)')
ylabel('Current (A)')
leg3 = legend('i_{batt}','location','best');
fig3_leg = findobj(leg1,'type','text');
set(fig3_leg,'FontSize',12)
set(gca,'FontSize',12)
grid on
print(gcf,'-dtiff','-r350','i_batt')
savefig('i_batt')

%% FFT plot of i_ems to show 60 and 180 Hz components

%---------------%
figure(10)
%---------------%

one_period=round(1/60/tstep);
v_ems_ss=v_ems(2/tstep:2/tstep+one_period,1); % data at t=4 seconds
v_ems_spect=fft(v_ems_ss)/(one_period/2);
plot(0,20*log10(abs(v_ems_spect(1))/2),'bo');  % DC component
hold on
plot(([2:40]-1),20*log10(abs(v_ems_spect(2:40))),'ro');
hold off
xlabel('Harmonic Number');
ylabel('i_{ems} [dB]');
```

```
%% LCDR Gabriel Hernandez, Thesis
%
% With assistance from:
% NPS Prof. Giovanna Oriti
% NPS Prof. Alexander Julian
% NPS Prof. Roberto Cristi
%
% Script to plot laboratory results

%% Clear variables and command window, and close all plots
clc;
clear all;
close all;

%% Import Excel spreadsheet data

% Charging, with 120 Hz ripple
vsx_ch120 = xlsread('Tek_CH1_Wfm_vs.csv');
iSCx_ch120 = xlsread('Tek_CH3_Wfm_iSC.csv');

% Charging, without 120 Hz ripple
vsx_chno120 = xlsread('Tek_CH1_Wfm_vs_no120.csv');
iSCx_chno120 = xlsread('Tek_CH3_Wfm_iSC_no120.csv');

% Discharging, with 120 Hz ripple
vsx_dis120 = xlsread('Tek_CH1_Wfm_vs_discharge.csv');
iSCx_dis120 = xlsread('Tek_CH3_Wfm_iSC_discharge.csv');

% Discharging, without 120 Hz ripple
vsx_disno120 = xlsread('Tek_CH1_Wfm_vs_no120_discharge.csv');
iSCx_disno120 = xlsread('Tek_CH3_Wfm_iSC_no120_discharge.csv');

%% Plot output data

% Charging, with 120 Hz ripple

len_ch120 = length(vsx_ch120);
time_vec_ch120 = vsx_ch120(15:len_ch120,1);
time_vec_ch120 = time_vec_ch120+.02; % Shift the time axis to start at
t = 0
vs_ch120 = vsx_ch120(15:len_ch120,2);
iSC_ch120 = iSCx_ch120(15:len_ch120,2);
tmin_ch120 = time_vec_ch120(1);
tmax_ch120 = max(time_vec_ch120);

figure(1);
plot(time_vec_ch120,vs_ch120/20,time_vec_ch120,-iSC_ch120);
xlabel('Time (s)')
ylabel('Volts (V) or Current (A)');
leg1 = ...
    legend('v_s/20','i_{scboost}','Location','Northeast');
fig1_leg = findobj(leg1,'type','text');
set(fig1_leg,'FontSize',12)
```

```
set(gca,'FontSize',12)
grid on;
axis([tmin_ch120 tmax_ch120 -8 8])
print(gcf,'-dtiff','-r350','Charging with 120 Hz ripple');

% Charging, without 120 Hz ripple

len_chno120 = length(vsx_chno120);
time_vec_chno120 = vsx_chno120(15:len_chno120,1);
time_vec_chno120 = time_vec_chno120+.02; % Shift the time axis to start
at t = 0
vs_chno120 = vsx_chno120(15:len_chno120,2);
iSC_chno120 = iSCx_chno120(15:len_chno120,2);
tmin_chno120 = time_vec_chno120(1);
tmax_chno120 = max(time_vec_chno120);

figure(2);
plot(time_vec_chno120,vs_chno120/20,time_vec_chno120,-iSC_chno120);
xlabel('Time (s)')
ylabel('Volts (V) or Current (A)');
leg2 = ...
    legend('v_s/20','i_{scboost}','Location','Northeast');
fig2_leg = findobj(leg2,'type','text');
set(fig2_leg,'FontSize',12)
set(gca,'FontSize',12)
grid on;
axis([tmin_chno120 tmax_chno120 -8 8])
print(gcf,'-dtiff','-r350','Charging without 120 Hz ripple');

% Discharging, with 120 Hz ripple

len_dis120 = length(vsx_dis120);
time_vec_dis120 = vsx_dis120(15:len_dis120,1);
time_vec_dis120 = time_vec_dis120+.02; % Shift the time axis to start
at t = 0
vs_dis120 = vsx_dis120(15:len_dis120,2);
iSC_dis120 = iSCx_dis120(15:len_dis120,2);
tmin_dis120 = time_vec_dis120(1);
tmax_dis120 = max(time_vec_dis120);

figure(3);
plot(time_vec_dis120,vs_dis120/20,time_vec_dis120,-iSC_dis120);
xlabel('Time (s)')
ylabel('Volts (V) or Current (A)');
leg3 = ...
    legend('v_s/20','i_{scboost}','Location','Northeast');
fig3_leg = findobj(leg3,'type','text');
set(fig3_leg,'FontSize',12)
set(gca,'FontSize',12)
grid on;
axis([tmin_dis120 tmax_dis120 -8 8])
print(gcf,'-dtiff','-r350','Discharging with 120 Hz ripple');

% Discharging, without 120 Hz ripple
```

```
len_disno120 = length(vsx_disno120);
time_vec_disno120 = vsx_disno120(15:len_disno120,1);
time_vec_disno120 = time_vec_disno120+.02; % Shift the time axis to
start at t = 0
vs_disno120 = vsx_disno120(15:len_disno120,2);
iSC_disno120 = iSCx_disno120(15:len_disno120,2);
tmin_disno120 = time_vec_disno120(1);
tmax_disno120 = max(time_vec_disno120);

figure(4);
plot(time_vec_disno120,vs_disno120/20,time_vec_disno120,-iSC_disno120);
xlabel('Time (s)')
ylabel('Volts (V) or Current (A)');
leg4 = ...
    legend('v_s/20','i_{scboost}','Location','Northeast');
fig4_leg = findobj(leg4,'type','text');
set(fig4_leg,'FontSize',12)
set(gca,'FontSize',12)
grid on;
axis([tmin_disno120 tmax_disno120 -8 8])
print(gcf,'-dtiff','-r350','Discharging without 120 Hz ripple');

% Additional plot to show effect of IGBT gating
figure(5);
plot(time_vec_chno120,-iSC_chno120,'r');
xlabel('Time (s)')
ylabel('Current (A)');
set(gca,'FontSize',12)
grid on;
axis([.0201 .0206 -4.5 -1])
print(gcf,'-dtiff','-r350','Charging without 120 Hz ripple');
```

THIS PAGE INTENTIONALLY LEFT BLANK

APPENDIX B. LABORATORY OUTPUT VALUES

Simulation Condition	SC Bank and Filter Usage	Battery Current Ripple Before Change (App)	Average Battery Current Before Change (A)	Reduction in Battery Current Achieved (%)	Reduction in Battery Current Achieved (%)	Battery Current Ripple After Change (App)	Average Battery Current After Change (A)	Reduction in Battery Current Achieved (%)	Reduction in Battery Current Achieved (%)	SC Bank Current Ripple Before Change (App)	SC Bank Current Ripple After Change (App)	Increase in SC Current Ripple Caused By Change (A)	Specifics
Grid connected, operator increases commanded current	SC bank disconnected	1.006	0.8264			3.9485	3.35845						Change at 10.0 sec EMS current changed from 1.0A to 4.0A System load = 10 ohms
	SC bank connected with 120 Hz BPF only	0.1013	0.82615	89.93%		0.399	3.4001	89.89%		2.8753	11.263	8.388	
	SC bank connected with 120 Hz BPF and LPF	0.0001	0.82615		99.99%	0.0003	3.35055		99.99%	3.0483	11.922	8.874	
Loss of AC grid source and transition to islanding mode	SC bank disconnected	1.0063	0.82645			17.0307	14.60035						Change at 5.0 sec Grid source removed System load = 10 ohms EMS commanded current = 1A
	SC bank connected with 120 Hz	0.1013	0.82615	89.93%		1.7623	14.81495	89.65%		2.8767	49.4784	46.602	
	SC bank connected with 120 Hz BPF and LPF	1E-04	0.82395		99.99%	0.0016	14.8303		99.99%	3.0443	52.1405	49.096	
Islanding, step increase in load	SC bank disconnected	2.3783	0.71485			17.0306	14.6003						Change at 5.0 sec System load increased from 200 ohms to 10 ohms EMS commanded current = 1A
	SC bank connected with 120 Hz BPF only	0.2408	0.714	89.88%		1.7627	14.81475	89.65%		6.8321	49.4786	42.647	
	SC bank connected with 120 Hz BPF and LPF	0.0002	0.714		99.99%	0.0015	14.82955		99.99%	7.2355	52.1406	44.905	

THIS PAGE INTENTIONALLY LEFT BLANK

LIST OF REFERENCES

[1] *Navy shore energy program* [Online]. Available: http://cnic.navy.mil/om/base_support/facility_system_investment/Navy_Shore_Energy_Program.html

[2] *U.S. Navy—energy, environment, and climate change* [Online]. Available: http://greenfleet.dodlive.mil/energy/

[3] F. Valencia, J. Collado, D. Sáez, and L. G. Marín, "Robust energy management system for a microgrid based on a fuzzy prediction interval model," *IEEE Transactions on Smart Grid,* vol. 7, pp. 1486–1494, 2016.

[4] P. Wang, J. Xiao, L. Setyawan, and C. F. Hoong, "Energy management system (EMS) for real-time operation of DC microgrids with multiple slack terminals," in *IEEE Power and Energy Society Innovative Smart Grid Technologies Conference Europe*, Istanbul, Turkey, 2014, pp. 1–6.

[5] R. BiYing, T. XiangQian, S. XiangDong, and Z. Qi, "Research on the control strategy of energy management system for low capability microgrid," in *IEEE Power Engineering and Automation Conference,* 2011, pp. 441–444.

[6] N. Piphitpattanaprapt and D. Banjerdpongchai, "Energy management system of hybrid power generation with battery energy storage and application to MHS smart grid project," in *54th Annual Conference of The Society of Instrument and Control Engineers of Japan,* Hangzhou, China, 2015, pp. 922–927.

[7] B. Lasseter, "Microgrids [distributed power generation]," in *Proceedings Power Engineering Society Winter Meeting,* 2001, pp. 146–149 vol.1.

[8] F. A. Farret and M. G. Simões, *Integration of Alternative Sources of Energy.* Piscataway, NJ: Wiley-IEEE Press, 2006.

[9] H. Fakham, D. Lu, and B. Francois, "Power control design of a battery charger in a hybrid active PV generator for load-following applications," *IEEE Transactions on Industrial Electronics,* vol. 58, pp. 85–94, 2011.

[10] N. R. Tummuru, M. K. Mishra, and S. Srinivas, "Dynamic energy management of renewable grid integrated hybrid energy storage system," *IEEE Transactions on Industrial Electronics,* vol. 62, pp. 7728–7737, 2015.

[11] G. Zhang, X. Tang, and Z. Qi, "Research on battery supercapacitor hybrid storage and its application in microgrid," in *Asia-Pacific Power and Energy Engineering Conference,* Chengdu, China*,* 2010, pp. 1–4.

[12] F. S. Garcia, A. A. Ferreira, and J. A. Pomilio, "Control strategy for battery-ultracapacitor hybrid energy storage system," in *Twenty-Fourth Annual IEEE Applied Power Electronics Conference and Exposition,* 2009, pp. 826–832.

[13] A. A. Ferreira, J. A. Pomilio, G. Spiazzi, and L. de Araujo Silva, "Energy management fuzzy logic supervisory for electric vehicle power supplies system," *IEEE Transactions on Power Electronics,* vol. 23, pp. 107–115, 2008.

[14] B. Hredzak, V. G. Agelidis, and M. Jang, "A model predictive control system for a hybrid battery-ultracapacitor power source," *IEEE Transactions on Power Electronics,* vol. 29, pp. 1469–1479, 2014.

[15] J. Shen, S. Dusmez, and A. Khaligh, "Optimization of sizing and battery cycle life in battery/ultracapacitor hybrid energy storage systems for electric vehicle applications," *IEEE Transactions on Industrial Informatics,* vol. 10, pp. 2112–2121, 2014.

[16] R. A. Dougal, S. Liu, and R. E. White, "Power and life extension of battery-ultracapacitor hybrids," *IEEE Transactions on Components and Packaging Technologies,* vol. 25, pp. 120–131, 2002.

[17] A. Lantero. (2014, June 17). *How microgrids work* [Online]. Available: http://www.energy.gov/articles/how-microgrids-work

[18] G. Oriti, A. L. Julian, and N. J. Peck, "Power-electronics-based energy management system with storage," *IEEE Transactions on Power Electronics,* vol. 31, pp. 452–460, 2016.

[19] Lijun Gao, R. A. Dougal, and Shengyi Liu, "Power enhancement of an actively controlled battery/ultracapacitor hybrid," *IEEE Transactions on Power Electronics,* vol. 20, pp. 236–243, 2005.

[20] H. El Brouji, J. M. Vinassa, O. Briat, N. Bertrand, and E. Woirgard, "Ultracapacitors self discharge modelling using a physical description of porous electrode impedance," in *IEEE Vehicle Power and Propulsion Conference,* 2008, pp. 1–6.

[21] I. Vechiu, A. Etxeberria, H. Camblong, and J. M. Vinassa, "Three-level neutral point clamped inverter interface for flow battery/supercapacitor energy storage system used for microgrids," in *2nd IEEE Power and Energy Society International Conference and Exhibition On Innovative Smart Grid Technologies Europe,* Manchester, UK, 2011, pp. 1–6.

[22] N. Kularatna, "Supercapacitors improve the performance of linear power-management circuits: unique new design options when capacitance jump from micro-farads to farads with a low equivalent series resistance," *IEEE Power Electronics Magazine,* vol. 3, pp. 45–59, 2016.

[23] M. Alsolami, J. Wang, and L. Herrera, “DC ripple current reduction on multilevel, multiport, single-phase DC/AC converter for renewable energy applications,” in *IEEE 3rd Workshop On Wide Bandgap Power Devices and Applications,* 2015, pp. 312–318.

[24] Y. Jin, T. Shimizu, and G. Kimura, “DC ripple current reduction on a single phase PWM voltage source converter,” in *Proceedings of the 24th Annual Conference of the IEEE Industrial Electronics Society,* Aachen, Germany, 1998, pp. 525–530 vol.1.

[25] W. Marańda, “Capacity degradation of lead-acid batteries under variable-depth cycling operation in photovoltaic system,” in *22nd International Conference “Mixed Design of Integrated Circuits and Systems,”* Toruń, Poland, 2015, pp. 552–555.

[26] A. S. Sedra and K. C. Smith, *Microelectronic Circuits.* New York: Oxford University Press, 1998.

[27] Byungcho Choi, *Pulsewidth Modulated DC-to-DC Power Conversion: Circuits, Dynamics, and Control Designs*. Piscataway, NJ: Wiley-IEEE Press, 2013.

[28] D. B. W. Abeywardana, B. Hredzak, and V. G. Agelidis, “Battery-supercapacitor hybrid energy storage system with reduced low frequency input current ripple,” in *International Conference on Renewable Energy Research and Applications,* Palermo, Italy, 2015, pp. 328–332.

THIS PAGE INTENTIONALLY LEFT BLANK

INITIAL DISTRIBUTION LIST

1. Defense Technical Information Center
   Ft. Belvoir, Virginia

2. Dudley Knox Library
   Naval Postgraduate School
   Monterey, California